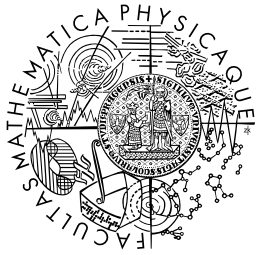

FACULTY
OF MATHEMATICS
AND PHYSICS
Charles University

MASTER THESIS

Daniel Král

Optical and magneto-optical properties of Heusler compounds

Institute of Physics of Charles University

Supervisor of the master thesis: RNDr. Martin Veis, Ph.D

Study programme: Physics

Study branch: Optics and Opto-electronics

Prague 2017

I declare that I carried out this master thesis independently, and only with the cited sources, literature and other professional sources.

I understand that my work relates to the rights and obligations under the Act No. 121/2000 Sb., the Copyright Act, as amended, in particular the fact that the Charles University has the right to conclude a license agreement on the use of this work as a school work pursuant to Section 60 subsection 1 of the Copyright Act.

In ..... date ..... signature of the author

Title: Optical and magneto-optical properties of Heusler compounds

Author: Daniel Král

Department: Institute of Physics of Charles University

Supervisor: RNDr. Martin Veis, Ph.D, Institute of Physics of Charles University

Abstract: The aim of this diploma thesis was to study the Heusler compounds using both optical and magneto-optical (MO) methods. In the case of the first compound, $Co_2FeGa_{0.5}Ge_{0.5}$, we have studied the presence of the structural disorder phenomena by the means of spectroscopic ellipsometry, MO spectroscopy and MO Kerr magnetometry. The experimental results were confronted with theoretical models. We have also provided the complementary results of our collaborators, including X-ray diffraction, atomic-force microscopy and ab initio calculations, in order to support our interpretation of obtained data. We have found that the structural disorder is indeed observable with the help of the methods we have employed. This was explained via the differences in the band structure of structurally ordered and disordered samples. In the case of the second compound, Fe_2MnGa, we have investigated the influence of the Fe content on the overall optical and MO properties of the material. We have found that the iron atoms influence free carrier concentration of the alloy making it metallic comparing to Ni_2MnGa and increasing optical and MO response in the near infrared region of the spectrum. The sample with the highest content of iron has been found to posses zero magnetization.

Keywords: Heusler compounds, magneto-optical spectroscopy, spectroscopic ellipsometry

First and foremost, I would like to thank RNDr. Martin Veis, Ph.D., Mgr. Jaroslav Hamrle, Ph.D. and Mgr. Lukáš Beran for all their guidance, advice and support. It has always been an honor for me to work with you guys and I can only thank you for making our laboratory a place that I actually love to return to.

I would also like to thank Enrique Vilanova, Petr Cejpek, Dr. Oleg Heczko and Dr. Josef Kudrnovský for contributing to this work. Your results have made it possible for me to produce my own.

Of course, most of all I would like to thank my family. This work would never have been written if it were not for your love and support.

Contents

Introduction

The Heusler compounds have gained significant amount of attention in the past years owing to high application potential. Because of the highly tunable electronic structure and extraordinary magneto-optical (MO), magnetoelectric, and magnetocaloric properties, Heusler compounds have found use in a vast number of research fields, including superconductivity [1], magnetic shape memory [2] and, most recently, topological insulators [3]. They have also proven to be more than suitable for utilization in spintronics because of the high spin polarization some of them exhibit [4].

In this work, two of these extraordinary materials have been studied. The first one is the recently synthesized $Co_2FeGa_{0.5}Ge_{0.5}$. This Co-based Heusler compound is being actively researched in present days because of its potential application in giant magnetoresistance devices, lateral spin valve-based reading heads and microwave assisted magnetic recording techniques. The second material is a magnetic shape memory alloy (MSMA), Fe_2MnGa, that has been synthesized in order to improve the functionality of the original MSMA, Ni_2MnGa. Because of the large magnetic shape memory effect they exhibit, the MSMAs are planned to be employed as sensors and actuators as well as active/passive vibration damping devices.

The MO methods are simple, yet powerful experimental techniques for the characterization of physical properties of materials. In the present, magneto-optics is regularly used for the real-time imaging of magnetic domains (Kerr microscopy), or the measurements of hysteresis loops (Kerr magnetometry). The main part of our research involves a combination of spectroscopic ellipsometry and MO spectroscopy. While the first experimental technique is a prominent and universal tool, the second one is its extension to the magnetic field-induced anisotropy region. When combined, these two methods may provide unique information about the electronic structure of the material. In addition, Kerr magnetometry has been employed as well. Being fast, contactless and non-destructive, optical and MO-based methods are the perfect instruments for investigating the Heusler compounds.

This work has been divided into five chapters. Chapter one contains the theoretical basis necessary for presented research, including basic wave optics, optical properties of materials and a description of the MO phenomena. The second chapter is primarily devoted to the general description of Heusler compounds. Their basic basic properties, such as composition, band structure and the rather important issue of structural disorder are mainly discussed. In the third chapter, we provide basic information about the particular compounds investigated in this work - the above-mentioned $Co_2FeGa_{0.5}Ge_{0.5}$ and Fe_2MnGa. The fourth chapter contains detailed description of the methods we have used for our research. Apart from spectroscopic ellipsometry and MO spectroscopy, Kerr magnetometry will also be discussed. Finally, the fifth chapter provides the results of our research. In the case of $Co_2FeGa_{0.5}Ge_{0.5}$, we have examined the manifestation of structural disorder in the optical and MO response of the samples. In the case of Fe_2MnGa, the research concerned the difference of this response between alloys with different composition.

1. Basic theory

1.1 Electromagnetic waves

The aim of this section is to introduce basic theoretical approaches employed in wave optics. These concepts will be necessary for the description of magneto-optical effects and understanding of physical properties of Heusler compounds. Firstly, we will describe the wave-like behavior of electromagnetic radiation. We shall discuss the physical processes that govern the electromagnetic waves and we will also present the basic relations between their components and characteristics. This will enable us to understand the polarization of light, which will be introduced in the next part. Understanding this phenomenon is important for the studies of the magneto-optical Kerr effect and we will, therefore, study it rather throughly.

In the last subsection, a mathematical model known as the Jones calculus will be introduced. It will be put to use throughout most of the chapters, mostly in chapter 4, which is devoted to the description of experimental techniques used in this work.

1.1.1 Basic wave optics

The wave equation

Firstly, we will show that it is possible for the electromagnetic field to propagate through space in a wave-like manner. Let us begin by writing down the Maxwell equations for media that are linear, isotropic and homogeneous in all properties and contain no free charge [5]. For the electromagnetic field, described by the vectors $\mathbf{E}$ and $\mathbf{B}$, the equations are as follows:

$$\nabla \cdot \mathbf{E} = 0\,, \tag{1.1}$$

$$\nabla \times \mathbf{E} = -\frac{\partial \mathbf{B}}{\partial t}\,, \tag{1.2}$$

$$\nabla \cdot \mathbf{B} = 0\,, \tag{1.3}$$

$$\nabla \times \mathbf{B} = \mu\mathbf{j} + \mu\varepsilon\frac{\partial \mathbf{E}}{\partial t}\,. \tag{1.4}$$

Here ε and μ are the permittivity and permeabilty of the medium.

For the sake of simplicity, we will assume that the medium is nonconducting and its conductivity σ is zero [6]. Employing Ohm's law,

$$\mathbf{j} = \sigma\mathbf{E}\,, \tag{1.5}$$

equation (1.4) becomes

$$\nabla \times \mathbf{B} = \mu\varepsilon\frac{\partial \mathbf{E}}{\partial t}\,. \tag{1.6}$$

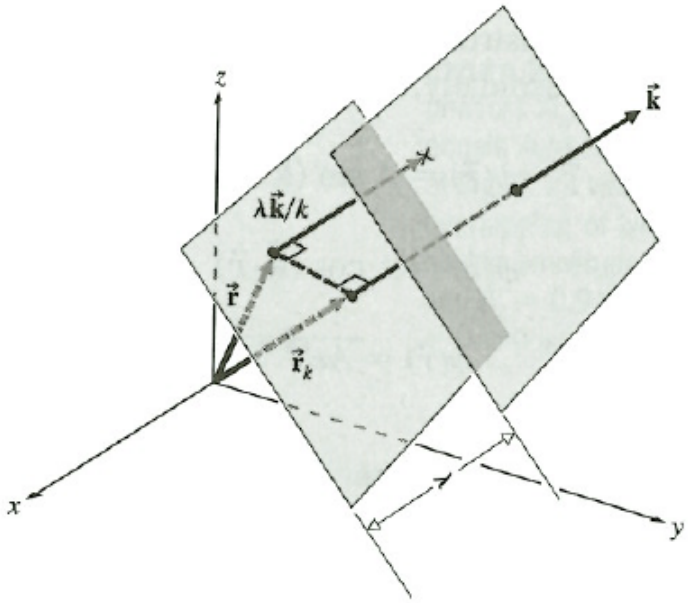

Figure 1.1: Propagation of plane waves through space. $\vec{k}$ is the wave vector, λ is the wavelength and $\vec{r}$ denotes the spatial vector with x, y and z as its components [7].

We will now derive the wave equation for the electric component of the electromagnetic field, noting that the same can be done for the magnetic component as well [5]. Applying the curl operator to equation (1.2), we get

$$\nabla \times (\nabla \times \mathbf{E}) = -\frac{\partial}{\partial t}(\nabla \times \mathbf{B})\,. \tag{1.7}$$

By employing the vector identity $\nabla \times (\nabla \times \mathbf{v}) = \nabla(\nabla \cdot \mathbf{v}) - \nabla^2\mathbf{v}$, where $\mathbf{v}$ is an arbitrary vector, and using equations (1.1) and (1.4), we obtain

$$\nabla^2\mathbf{E} = \mu\varepsilon\frac{\partial^2\mathbf{E}}{\partial t^2}\,. \tag{1.8}$$

Equation (1.8) is a hyperbolic partial differential equation. Equations of this type are used for the description of wave motion and, therefore, this particular one describes the wave-like motion of the electric field.

The product of μ and ε defines the velocity of propagation of the electromagnetic wave in a given medium,

$$\mu\varepsilon = \frac{1}{v}\,, \tag{1.9}$$

which follows from the general form of the wave equation.

Plane waves

Now, let us discuss a solution of equation (1.8) in its simplest form - the harmonic plane wave [7]. All wavefronts of a plane wave are infinite parallel planes that are

perpendicular to the direction of propagation (see figure 1.1). In this form, the solution of equation (1.8) and its magnetic counterpart is

$$\mathbf{E} = \mathbf{E}_0 e^{i(\mathbf{kr}-\omega t+\delta)}\,, \tag{1.10}$$

$$\mathbf{B} = \mathbf{B}_0 e^{i(\mathbf{kr}-\omega t+\delta)}\,. \tag{1.11}$$

Here ω is the wave's angular frequency, $|\mathbf{k}| = \frac{\omega}{v}$ is the so-called wave vector and δ is the initial phase of the wave. $\mathbf{E}_0$ and $\mathbf{B}_0$ are spatially and temporarily independent vector amplitudes of electric and magnetic fields.

The spatial periodicity of waves can be described by its wavelength λ - the distance between the two closest points on the wave that have the same phase. Let us also define the refraction index,

$$n = \frac{c}{v}\,, \tag{1.12}$$

as a ratio of the wave's velocity in a vacuum, c, and its velocity in a given medium, v. It is convenient to mention that through equation (1.9), $\mathbf{v}$ (and therefore n) is directly connected to the optical properties of matter described by μ and ε. It should be noted, however, that one usually has to deal only with the electric component of the field. Including μ in the theoretical models is, therefore, unnecessary in most cases.

Let us also write down some basic relations between the above-mentioned quantities:

$$|\mathbf{k}| = \frac{2\pi}{\lambda} = \frac{n\omega}{c} = \frac{\omega}{v}\,. \tag{1.13}$$

Should the reader be interested in the detailed derivation of these relations, it can be found in [8], or any other optical handbook.

For a plane wave, it can be shown that the vectors $\mathbf{E}$, $\mathbf{B}$ and $\mathbf{k}$ form an orthogonal system. Substituting expressions (1.10) and (1.11) to equations (1.1) through (1.4), one finds that

$$\mathbf{E} = -\frac{|\mathbf{v}|^2}{\omega}\mathbf{k} \times B \tag{1.14}$$

and

$$\mathbf{B} = \frac{1}{\omega}\mathbf{k} \times E\,. \tag{1.15}$$

Considering the properties of vector multiplication, one can directly see from (1.14) and (1.15) that both $\mathbf{E}$ and $\mathbf{B}$ are perpendicular to $\mathbf{k}$. Since $\mathbf{k}$ is parallel to the direction of propagation, this means that the electromagnetic waves are transverse. For more details, see [5] or [9].

1.1.2 Polarization

Polarized and unpolarized light

Each vectorial wave has an intrinsic property called polarization. In the case of electromagnetic radiation, this property specifies the direction of the oscillations of the field vectors, $\mathbf{E}$ and $\mathbf{B}$.

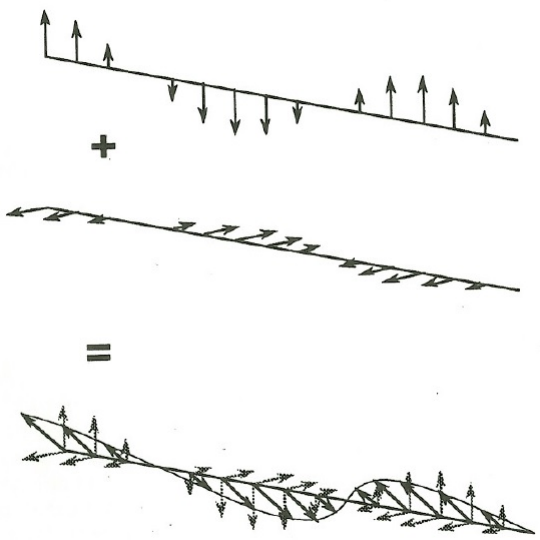

Figure 1.2: Two linearly polarized light beams of the same phase and amplitude form a third one by the means of superposition [10].

Let us imagine the simplest case, in which $\mathbf{E}$ oscillates in one plane. We refer to this kind of polarization as the linear polarization. Let $\mathbf{E}_1(\mathbf{r}, t)$ and $\mathbf{E}_2(\mathbf{r}, t)$ be two orthogonally linearly polarized beams of equal amplitude. If $\Delta\delta = \delta_1 - \delta_2$ is their phase difference then for $\Delta\delta = 0$, the two beams will create a linearly polarized beam (see figure 1.2). This beam has its linear polarization tilted by $45°$ with respect to the original pair. If $\Delta\delta$ is precisely $90°$, the resultant light beam will have its components oscillating in a circle, when looked upon frontally. We shall refer to this beam as being circularly polarized.

For $\Delta\delta$ is an arbitrary, we obtain an elliptically polarized beam. This case is the most general one for strictly monochromatic optical fields [11] and we shall now describe it in more detail.

Elliptic polarization

When a linearly polarized light beam is reflected from the surface of a conductive material, the reflected part of the beam becomes generally elliptically polarized. Analysis of the parameters of the polarization ellipse yields information about the material's composition, electronic structure, roughness of its surface, etc. The theories concerning these changes in polarization are, therefore, vividly employed in material science and optics [11].

To describe the polarization ellipse mathematically, one can restrict themselves to only four parameters. It is important to note that there are several choices of parameters, which one can use. Moreover, there is a certain freedom in the choice of the sign convention (some angles can be defined with either positive, or negative sign).

These two facts lead to the polarization parameters being defined differently by almost every author. One must, therefore, proceed rather carefully when referring to results from different handbooks. Here, we choose the definitions listed in [12] as all the magneto-optical theory in this work is deduced from this

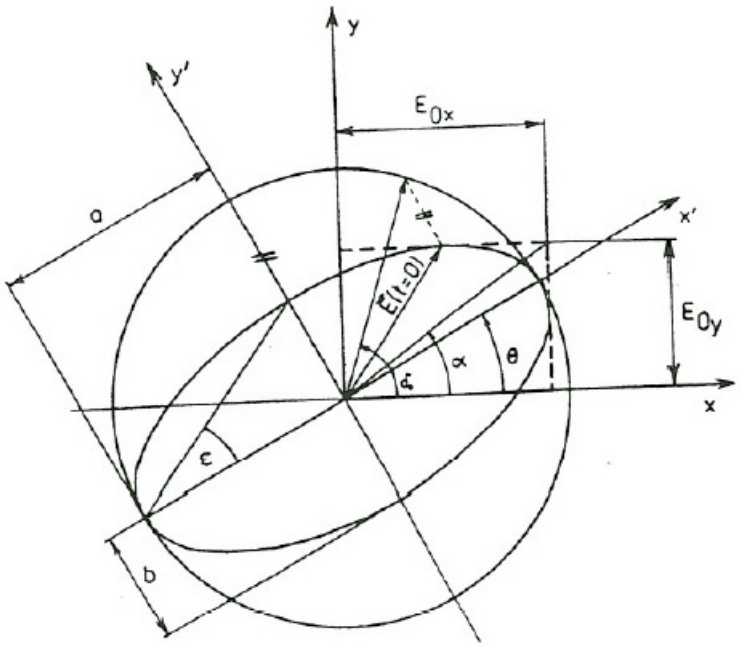

Figure 1.3: The polarization ellipse with a denoting the semi-major and b denoting the semi-minor axis. Here E_{0x} and E_{0y} are the components of electric intensity $\vec{E}$. The polarization parameters, azimuth and ellipticity, are denoted by θ and ϵ [14]

literature.

Figure 1.3 provides the frontal view of the polarization ellipse, as well as the parameters describing it. These parameters can be defined as follows:

- θ is the angle between the major axis and the positive direction of x. This is the so-called *azimuth* and it is limited to $\left\langle -\frac{\pi}{2}, \frac{\pi}{2} \right)$.
- *Ellipticity* e is the ratio of the semi-minor and semi-major axis of the ellipse, $e = \frac{b}{a}$. It is convenient to define the ellipticity angle ϵ, so that $e = \tan\epsilon$, where $\epsilon \in \left\langle -\frac{\pi}{4}, \frac{\pi}{4} \right\rangle$.
- The measure of strength of the elliptical vibration is defined by the *amplitude* $E_{00} = \sqrt{a^2 + b^2}$.
- The angle δ_0 is the *absolute phase* and it is the angle between the vector $\mathbf{E}$ at the initial time ($t = 0$) and the major axis of the ellipse.

For our purposes, all four parameters will be necessary - the first pair will be put to use in the studies of magneto-optical effects, while the second one will be used in the mathematics of spectroscopic ellipsometry.

1.1.3 The Jones formalism

The Jones vectors

In practice it is often necessary to describe the effect of optical elements on the polarization of the light beam. For this purpose, we will now introduce a simple

mathematical apparatus called the Jones calculus. It should be noted, however, that there are several formalisms at hand - namely the illustrative Poincaré sphere, or the Stokes formalism developed for handling partially polarized light (should the reader be interested, a detailed explanation is given in [7]). Developed in 1941 by R. C. Jones, the Jones formalism is a practical and simple representation of polarized monochromatic light. Unlike the Stokes calculus it only deals with polarized waves.

Firstly, let us define the so-called Jones vectors [1]. Choosing the coordinate axis z to be parallel to the direction of propagation, the electric component of the plane wave can be written as

$$\mathbf{E}(z,t) = \begin{bmatrix} E_x(z,t) \\ E_y(z,t) \end{bmatrix}. \tag{1.16}$$

Let us now proceed to simplifying vector (1.16) to a more convenient form. Firstly, we shall exclude the frequency from our model, since there is no need for it in the description of polarization changes. Secondly, we shall restrict to only one transverse plane - for instance $z = 0$. At this point equation (1.16) takes the form of

$$\mathbf{E} = \begin{bmatrix} E_x e^{i\delta_x} \\ E_y e^{i\delta_y} \end{bmatrix}, \tag{1.17}$$

δ_x and δ_y being the respective phases.

Finally, we shall normalize the vectors to unity, so that

$$|\mathbf{J}|^2 = J^\dagger J = JJ^\dagger = \mathbf{1} \tag{1.18}$$

for all Jones vectors $\mathbf{J}$. Normalization is justifiable for applications where the exact information about amplitudes and phases is not necessarily needed [7].

The Jones vectors are defined in a two-dimensional complex vector space. There is, in principle, an infinite number of basis to this space [13], the most commonly used being the Cartesian basis and the circular basis.

The Cartesian basis is composed of two perpendicular linear polarizations

$$\mathbf{E_x} = \begin{bmatrix} 1 \\ 0 \end{bmatrix}, \quad \mathbf{E_y} = \begin{bmatrix} 0 \\ 1 \end{bmatrix}. \tag{1.19}$$

The circular basis is composed of two circular polarizations with an opposite orientation. With respect to the Cartesian basis, the vectors take the form of

$$\mathbf{E_R} = \frac{1}{\sqrt{2}} \begin{bmatrix} 1 \\ i \end{bmatrix}, \quad \mathbf{E_L} = \frac{1}{\sqrt{2}} \begin{bmatrix} 1 \\ -i \end{bmatrix}. \tag{1.20}$$

Any polarization can now be decomposed between these pairs of vectors [7].

Let us note that the basal vectors of (1.19) are often chosen as p-polarized and s-polarized. E_p denotes polarization in the plane of incidence and E_s polarization perpendicular to this plane.

[1] It is convenient to only use $\mathbf{E}$ in order to describe optical fields. If needed, $\mathbf{B}$ can always be calculated from (1.15).

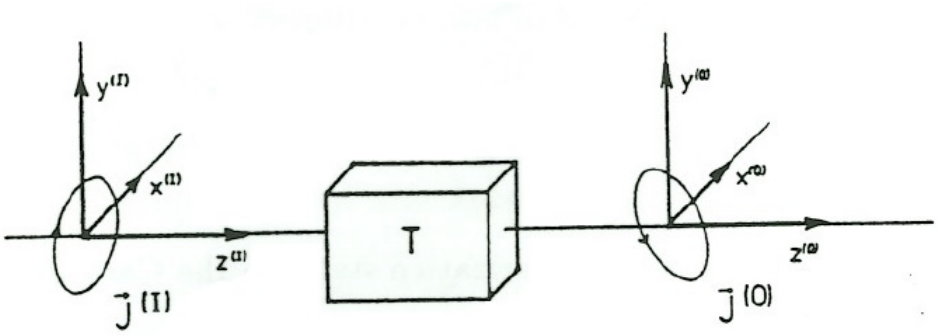

Figure 1.4: The elliptically polarized light propagates in the direction of the z-axis, described by the Jones vector $\mathbf{J}_I$. Upon entering the polarizing optical system described by the Jones matrix T, the polarization state changes to $\mathbf{J}_O$ [14].

The Jones matrices

We shall continue by describing elements that can change the polarization vector. In the Jones calculus, any of the optical elements (polarizers, waveplates, etc.) is represented by a 2x2 complex matrix. If $\mathbf{J}_I$ is the Jones vector of the light beam entering the polarizing system and $\mathbf{J}_O$ is the vector of the beam leaving it, then

$$\mathbf{J}_O = \mathbf{T}\mathbf{J}_I \,, \tag{1.21}$$

where $\mathbf{T}$ is the Jones matrix that represents the system (see figure 1.4).

A polarizing optical setup composed of N elements is described by a product of the respective Jones matrices,

$$\mathbf{T} = \Pi_{i=N}^{1}\mathbf{T}_i = \mathbf{T}_N\mathbf{T}_{N-1}...\mathbf{T}_1 \,, \tag{1.22}$$

where $\mathbf{T}_1$ is the matrix of the first component in the system and $\mathbf{T}_N$ is the matrix of the last one [14]. Multiplying the matrices in such sequence will preserve the order in which the light passes through the respective elements.

Before we proceed to specifying Jones matrices for the most frequently used components, we shall mention two important details. Firstly, every Jones matrix is always defined relatively to the polarization basis - in the following we shall always use the Cartesian basis (1.19). Secondly, the orientation of the optical elements with respect to the coordinate system should not be overlooked. Should the elements be rotated by some angle, their matrices should be transformed using the rotation matrix (as described in [14])

Here are the most important examples of the Jones matrices:

- A linear polarizer rotated by an angle α:

$$\mathbf{P}_\alpha = \begin{bmatrix} \cos^2\alpha & \cos\alpha\sin\alpha \\ \cos\alpha\sin\alpha & \sin^2\alpha \end{bmatrix} . \tag{1.23}$$

- A waveplate with a phase shift δ:

$$\mathbf{R}_\delta = \begin{bmatrix} e^{i\delta/2} & 0 \\ 0 & e^{-i\delta/2} \end{bmatrix} . \tag{1.24}$$

- A reflective surface:

$$\mathbf{Z} = \begin{bmatrix} 1 & 0 \\ 0 & -1 \end{bmatrix} . \tag{1.25}$$

In summary, when treating an optical polarizing system, we first need to calculate the Jones matrix of said system with the help of (1.22). Then, using equation (1.21), we apply this matrix to the known vector $\mathbf{J}_I$ (usually chosen to be linearly polarized). Obtaining $\mathbf{J}_O$, we can now proceed to calculating the intensity[2] of the light beam propagating through the system,

$$I_O \approx \frac{1}{2}\mathbf{J}_O^\dagger \mathbf{J}_O \, . \tag{1.26}$$

1.2 Optical properties of matter

In this section, we will describe the way matter behaves when exposed to electromagnetic radiation. The theory described will be necessary for the description of both optical and magneto-optical phenomena.

We shall start by defining the permittivity tensor. As it was explained in the previous part, light can be viewed as a harmonic disturbance of the electromagnetic field. Electromagnetic properties of matter are fully described by its permittivity and permeability. However, when dealing with the interaction of light and matter, one finds that permeability can be excluded from the theoretical models - at optical frequencies the interaction between electromagnetic radiation and electron spins is negligible [14]. Permittivity, on the other hand, affects all kinds of various optical properties of materials, from dichroism to refraction [15]. We will confine to study only the phenomena relevant to this work.

In the next part, we will list the basic mathematical models explaining the response of materials to radiation. There is a vast number of theories concerning this topic and we will only explain the most essential approaches - the Lorentz model and the Drude model.

Finally, we shall present a microscopic view on the interaction between light and matter. We will explain the basics of the band theory of solids and use them to discuss the optical absorption via interband transitions. We will also include a definition of the density of states to illustrate the half-metallic behavior of Heusler compounds.

[2] In common optical measurements one cannot directly measure polarization - a combination of polarizing elements and intensity detectors has to be used.

1.2.1 The permittivity tensor

Although we considered permittivity to be a scalar in the first parts, it is in fact a second rank tensor (sometimes called the dielectric tensor). In the Cartesian system, it is represented by the matrix

$$\varepsilon = \begin{bmatrix} \varepsilon_{xx} & \varepsilon_{xy} & \varepsilon_{xz} \\ \varepsilon_{yx} & \varepsilon_{yy} & \varepsilon_{yz} \\ \varepsilon_{zx} & \varepsilon_{zy} & \varepsilon_{zz} \end{bmatrix} . \tag{1.27}$$

Each of the components has both a real and an imaginary part. The tensor is therefore fully described by 18 quantities in total. However, from the Poynting theorem[3],

$$\nabla \cdot \mathbf{S} + \frac{\partial \mathbf{w}}{\partial t} = 0 \,, \tag{1.28}$$

it can be shown that the components of the permittivity tensor must satisfy the condition

$$\varepsilon_{ij} = \varepsilon_{ji} \,. \tag{1.29}$$

The tensor is then represented by a symmetric matrix

$$\varepsilon = \begin{bmatrix} \varepsilon_{xx} & \varepsilon_{xy} & \varepsilon_{xz} \\ \varepsilon_{xy} & \varepsilon_{yy} & \varepsilon_{yz} \\ \varepsilon_{xz} & \varepsilon_{yz} & \varepsilon_{zz} \end{bmatrix} . \tag{1.30}$$

This symmetry reduces the 18 independent variables to only 12 (for a detailed derivation, see [8] or [15]).

For optically anisotropic media, off-diagonal parts of (1.30) are generally non-zero. In magneto-optics, the optical anisotropy is induced by magnetic fields and the number of variables can be reduced to four by a suitable configuration of the magnetic field and the material (see sections 1.3 and 4.2).

For optically isotropic media, the diagonal elements are equal and the off-diagonal ones become zero. Thus, (1.30) becomes a diagonal matrix composed of only two independent variables. This is the case for the measurements conducted with the help of spectroscopic ellipsometry (section 4.1).

1.2.2 The spectral dependency of permittivity

The Lorentz model

The response of matter to radiation is generally dependent on the wavelength of the incoming electromagnetic wave. In 1878, H. A. Lorentz introduced a tool for calculating the physical quantities that govern optical processes in materials. This so-called Lorentz model is almost as simple as it is illustrative and is nowadays used as a basic principle for modeling the optical response.

This model views light as a harmonic disturbance to a system of electric dipoles. Let us now assume that matter is composed solely of atomic cores and

[3]Here $\mathbf{w}$ is the density of energy carried by the electric field and $\mathbf{S}$ is the Poynting vector.

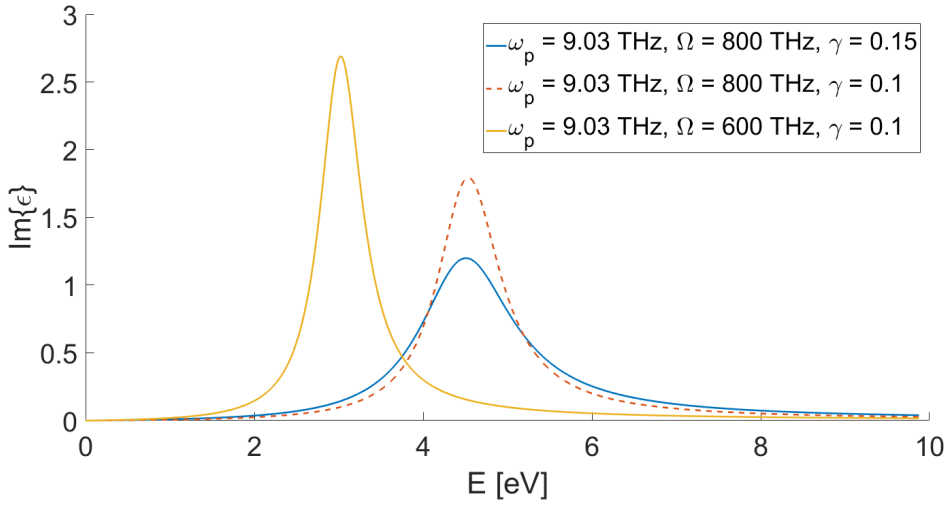

Figure 1.5: Examples of the Lorentzian peak described by the equation (1.38). The frequency of the probing radiation is given in eV. Sets of varying parameters described in the legend have been substituted to equation (1.38) in order to demonstrate the influence of each parameter on the shape bandwidth and amplitude of the peak. ω_p is the so-called plasma frequency defined by equation (1.40).

electrons, every electron being paired with only one of these cores. Each dipole possesses a dipole moment given by

$$\mathbf{p} = q\mathbf{x}\,. \tag{1.31}$$

The mass of electrons is more than a thousand times smaller than the mass of protons and it is therefore reasonable to assume that the cores will remain motionless relatively to their respective electrons.

The electron is bound to the core by a force that increases linearly with distance, just like in the case of a linear harmonic oscillator. Let us note that this representation of the binding force is only an approximation used for the first-order phenomena. By adding contributions of higher order (quadratic, cubic, etc.) to this force, we would get a model describing higher-order optical effects.

Using classical mechanics, the motion of the electron brought about by the electric force is given by the equation [4]

$$m\ddot{x} + m\gamma\dot{x} + \kappa x = qE\,. \tag{1.32}$$

Here m is the mass of the electron, γ is the damping factor and κ is the "rigidness" of the electron-core bond [15].

The electric force takes the shape of

$$E(t) = E_0 \exp[-i\omega t]\,. \tag{1.33}$$

It is reasonable to assume that the dipole will be oscillating with the same frequency as the electromagnetic field and we can therefore search for a solution

[4] Assuming the vector of the field $\mathbf{E}$ is parallel to x and denoting it simply as E

of (1.32) in form of

$$x(t) = x_0 \exp[-i\omega t]\,. \tag{1.34}$$

Substituting this solution into (1.32) we get

$$x_0 = \frac{qE_0}{m}\frac{1}{\Omega^2 - \omega - i\omega\gamma}\,, \tag{1.35}$$

where $\Omega^2 = \frac{\kappa}{m}$ is the square of the resonant frequency . Equation (1.35) represents the maximum distance the electron can get to before being drawn back to the core. We can now connect this amplitude to a physical quantity - polarization $\mathbf{P}$. For N identical electric dipoles the polarization is given by $\mathbf{P} = N\mathbf{p} = Nq\mathbf{x}$.

Through the calculation of electric susceptibility, we get

$$\varepsilon = 1 + \frac{Nq^2}{\varepsilon_0 m}\frac{\Omega^2 - \omega^2 + i\omega\gamma}{(\Omega^2 - \omega^2)^2 + \omega^2\gamma^2}\,. \tag{1.36}$$

Should the reader be interested in a more detailed derivation, a rather thorough one is given in [15].

It is convenient to separate the real and imaginary parts of this function as

$$\Re\{\varepsilon\} = \frac{Nq^2}{\varepsilon_0 m}\frac{\Omega^2 - \omega^2}{(\Omega^2 - \omega^2)^2 + \omega^2\gamma^2} + 1\,, \tag{1.37}$$

$$\Im\{\varepsilon\} = \frac{Nq^2}{\varepsilon_0 m}\frac{i\omega\gamma}{(\Omega^2 - \omega^2)^2 + \omega^2\gamma^2}\,. \tag{1.38}$$

Equations (1.37) and (1.38) are a very important result that fits surprisingly well to the permittivity spectra of various types of materials. If plotted against frequencies, function (1.38) takes the shape of the famous Lorentz curve, having a peak at the resonant frequency Ω (see figure 1.5). We will later use this model to fit the experimental data obtained by spectroscopic ellipsometry.

The Drude model

The reasons for electric conductivity lie in the mobility of the electron gas present in the material. The so-called conductive electrons are, in theory, able to move through the crystal freely. This can easily be embodied in the previous approach by simply setting $\kappa = 0$, therefore making the attractive force $\mathbf{F} = \kappa\mathbf{x}$ zero. Through this, the resonant frequency Ω also becomes zero, which we can now simply substitute to equation (1.36):

$$\varepsilon = 1 - \frac{Nq^2}{\varepsilon_0 m}\frac{\omega^2 - i\omega\gamma}{\omega^4 + \omega^2\gamma^2} = 1 - \frac{\omega_p^2}{\omega}\frac{\omega - i\gamma}{\omega^2 + \gamma^2}\,. \tag{1.39}$$

Here

$$\omega_p = \sqrt{\frac{Nq^2}{\varepsilon_0 m}} \tag{1.40}$$

is the so-called plasma frequency which for most metals is in the order of 10^{16} Hz [15]. For a detailed physical explanation of ω_p, see [16].

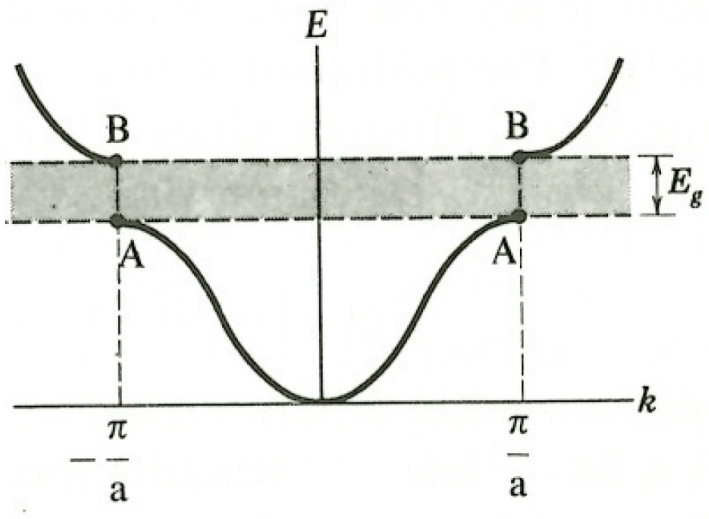

Figure 1.6: A simplified view of the band structure in the parabolic approximation [16]. Here k and E denote the wavevector and energy, respectively, while E_g stands for the width of the forbidden energies. A and B are denote the valence and conduction band.

The Drude model is used predominantly when describing materials with a large concentration of free carriers, such as metals. However, from (1.38) we can directly see that for $\Omega = 0$ Hz, $\Im\{\varepsilon\}$ diverges, which is quite inconvenient. To describe the absorption properties of metals, one often confines to the optical conductivity σ, rather than ε.

1.2.3 Quantum theory of optical processes

Energy bands

We shall now proceed to more advanced theories of the optical response. However, before getting to the interaction of light and matter, we first need to define the basic quantum-mechanical concepts of material science. We will start by discussing the possible energy states for electrons in solid state matter[5].

When solving the Schrödinger equation for an electron in a Coulomb potential (originating from an atomic core), one finds that the energy states create a discrete spectrum. Let us now increase the number of nearby cores to a larger amount. The electron becomes affected by the potentials of other cores, which brings more available states into the spectrum - the energy levels begin to overlap [19].

Solids contain about 10^{23} atomic cores in a cubic centimeter. Therefore, the amount of sublevels to an energy "level" in a cubic centimeter of crystallized matter is roughly of the same order. These sublevels are packed tightly together creating a quasi-continuous spectrum of allowed and forbidden energies (the so called energy bands and band gaps) [20].

The bands are either vallence or conductive (see figure 1.6). Vallence bands contain electrons that are bound to their respective cores and cannot move freely through the crystal. The electrons belonging to the conductive band are, on

[5]For the basics of quantum theory, see for instance [17] or [18]

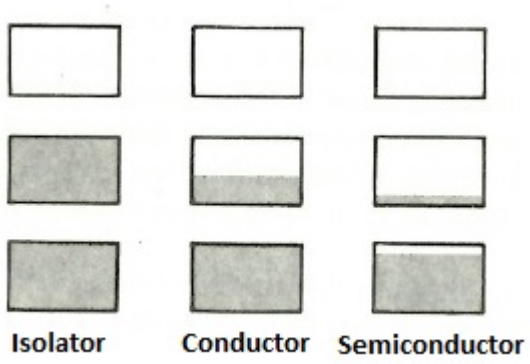

Figure 1.7: Materials with different transport characteristics as viewed by the band theory [16]. The isolators have their valence bands filled with the forbidden energy band too wide to posses any free carriers. The conductors posses a significant amount of free electrons around the Fermi energy, while the semiconductors may have free carriers injected into the conductive band from the valence one.

the other hand, able to travel through to crystal and participate in conducting electric currents. If given enough energy, electrons can overcome the band gap and travel from the vallence band to the conductive one.

Types of conductivity

Based on the band theory, we can now divide solid state matter into three basic groups based on its conductive properties (see figure 1.7):

- **Insulators** - For a material with a large gap (more than 4 eV) the electrons have no way of gaining enough energy to get to a conductive state, hence, under natural conditions, the material does not conduct electric current.
- **Semiconductors** - If a band gap is small enough (from 0.1 eV to 2 eV), electrons can, under certain conditions, pass to the conductive band. These conditions include a rise in the temperature of the crystal or the interaction with electromagnetic radiation.
- **Conductors** - For this type of solid state matter, the Fermi level lies inside the conductive band. There is, therefore, a large portion of electrons able to move the charge through the crystal.

  For more details, see [19].

Interband transitions

We will now discuss the semi-classical theory of interband transitions. Firstly, let us note that in this approach, light will be viewed as an electromagnetic wave, while matter will be described in a quantum-mechanical manner - hence the word ”semi-classical”. Also, we shall only be treating direct band transition.

The probability that the electron will transfer from the valence state $|i\rangle$ to a conductive state $|f\rangle$ can be calculated[6] using the Fermi Golden Rule

$$P_{i\to f} = \frac{2\pi}{\hbar}|\langle i|\hat{H}|f\rangle|^2\delta(E_f - E_i - \hbar\omega)\,. \tag{1.41}$$

Here δ is the Dirac δ-function and $\hat{H}$ is the Hamiltonian of the system, which, in the direct calculation of (1.41) can be replaced by a so-called interaction Hamiltonian, H_i. In a Coulomb gauge and for a monochromatic wave, the interaction Hamiltonian is

$$\hat{H}_i = -\frac{e}{m}\mathbf{p}\cdot\mathbf{A}\,, \tag{1.42}$$

where $\mathbf{A}$ is the oscillating vector potential of the electromagnetic wave.

The initial and final states of the electron are both in a form of a Bloch wave[7] of a corresponding energy band,

$$|i\rangle = u_{v,k_v}(\mathbf{r})\exp(i\mathbf{k_v}\cdot\mathbf{r})\,, \tag{1.43}$$

$$|f\rangle = u_{c,k_c}(\mathbf{r})\exp(i\mathbf{k_c}\cdot\mathbf{r})\,, \tag{1.44}$$

where $u(\mathbf{r})$ denotes a periodic function.

Using (1.41-1.44), we can now calculate

$$P_{tot} = \sum_{i,f} P_{i\to f}\,, \tag{1.45}$$

which is the total probability of the transition. In order to do so, we shall assume that the wavelength of the electromagnetic perturbation is far larger than the proportions of the system and the wave appears to be independent of the spatial coordinates (thus it is possible to exclude it from the integration in (1.45)). This is the so-called electric dipole approximation.

We shall also assume that the momentum of the photon can be neglected and it will not affect the momentum of the electron. This has already been mentioned above as this condition is necessary for band transitions that are direct.

The calculation of (1.45) then results in

$$P_{tot} = \frac{2\pi}{\hbar}\frac{eE_0}{2\omega m}\sum_k |p_{cv}|^2\delta(E_f - E_i - \hbar\omega)\,, \tag{1.46}$$

where p_{cv} is a material constant [21].

We shall now proceed by connecting microscopic quantities with their macroscopic projections. The total power loss in a unit volume of the material, W_{tot}, is given by

$$W_{tot} = \hbar\omega P_{tot}\,. \tag{1.47}$$

With the help of Beer's law we get

$$W_{tot} = \frac{\varepsilon_0\omega}{2}|E_0|^2\Im\{\varepsilon\}\,. \tag{1.48}$$

[6]For short enough relaxation times.

[7]See [16], [19], [20], [21] or any other textbook concerning solid state matter.

Using (1.48) with (1.46) we finally get

$$\Im\{\varepsilon\} = \frac{e^2\pi}{\varepsilon_0\omega^2 m^2}\sum_k |p_{cv}|^2\delta(E_f - E_i - \hbar\omega)\,. \tag{1.49}$$

As it was mentioned above, $\Im\{\varepsilon\}$ represents a physical quantity that is used to describe absorption of matter. From its spectral dependency we can see transitions between the energy bands a therefore indirectly observe the electronic structure of the material.

Density of states

When describing materials in a condensed state, one often refers not only to their band structure, but also to the degeneracy of the energy levels. This property can be represented easily by a quantity called the density of states (abbreviated as DOS), which is simply a number of allowed states per unit energy

$$g(E) = \frac{dN}{dE}\,, \tag{1.50}$$

This quantity is sometimes also defined as

$$g(E) = \sum_k \delta(E - E_k)\,, \tag{1.51}$$

where k labels all the possible states at energy E_k. For more details, see [20] or [21].

DOS is, for most cases, the same for all electrons. For a specific type of materials, however, the DOS varies for electrons with a different spin. This significantly affects the conductive properties of the material. For instance, it can behave as a semiconductor for spin-down electrons and a conductor for spin-up electrons, as seen on figure 1.8. These are the so-called half-metals and their properties will be studied thoroughly in chapter 2.

1.3 Magneto-optical effects

After laying down the basic principles concerning the light-matter interaction, we are now able to proceed to studying particular applications of these concepts.

Many magnetized materials gain the ability to change the polarization of the interacting light, either upon reflection (magneto-optical Kerr effect) or transmission (Farraday and Voigt effects) [12]. Studying these effects yields information about the magnetization of the material and can therefore be used to measure its hysteresis loops, domain structure, etc. Thus, magneto-optical (MO) methods have been established as a valuable research tool in the magnetism field.

This section is devoted to describing the mathematics of the most prominent MO effect - the magneto-optical Kerr effect (MOKE). Firstly, we shall extend the concept of permittivity to magnetized matter. This will enable us to define its reflection matrix and will ultimately lead to the introduction of measurable MOKE parameters, the Kerr rotation and Kerr ellipticity.

Secondly, we will define a set of different MO configurations. The geometry of the incident light, the material sample and the magnetic field substantially

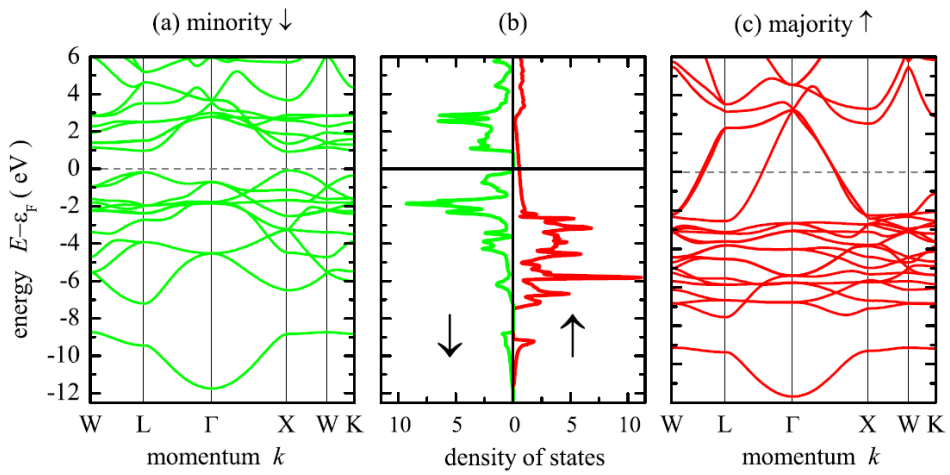

Figure 1.8: The calculated spin-resolved DOS of a half-metallic Heusler compound Co_2FeSi [22]. The DOS for minority-spin electrons is located on the left side (green), while the DOS for majority-spin electrons is on the right side (red). The respective band structures are presented on the sides of the figure.

changes the effect and different orientations are used in order to gain various information.

In the last part, we will characterize the various types of MOKE. The effect can be either linear or quadratic in magnetization and a detailed explanation of both will be presented by introducing the linear and quadratic MO tensors.

1.3.1 Light and magnetized media

Permittivity and magnetization

As it was explained in section 1.2, the elements of tensor (1.30),

$$\varepsilon = \begin{bmatrix} \varepsilon_{xx} & \varepsilon_{xy} & \varepsilon_{xz} \\ \varepsilon_{xy} & \varepsilon_{yy} & \varepsilon_{yz} \\ \varepsilon_{xz} & \varepsilon_{yz} & \varepsilon_{zz} \end{bmatrix},$$

can be further reduced under certain conditions. Let us consider an optically isotropic medium that is subjected to a uniform time-independent magnetic field. By choice, the z - axis will be parallel to the direction of magnetization. Due to the symmetry of the system[8], the tensor is invariant to all rotations around the z-axis.

The rotation about the z - axis is represented by the rotation matrix,

$$R(\theta) = \begin{bmatrix} \cos\theta & -\sin\theta & 0 \\ \sin\theta & \cos\theta & 0 \\ 0 & 0 & 1 \end{bmatrix}, \tag{1.52}$$

considering a counter-clockwise rotation by an arbitrary angle θ. Tensor (1.30)

[8]The symmetry group being $C_{\infty h}$ [12].

can only be invariant to this operation in the form

$$\varepsilon = \begin{bmatrix} \varepsilon_{xx} & \varepsilon_{xy} & 0 \\ -\varepsilon_{xy} & \varepsilon_{xx} & 0 \\ 0 & 0 & \varepsilon_{zz} \end{bmatrix} . \tag{1.53}$$

The permittivity tensor must also be invariant to the reversal of time. According to [23], the time reversal is in this case equal to reversing the magnetization vector[9]. As it is explained in [12] and [14], this leads to the so-called Onsager relation,

$$\varepsilon_{ij}(\mathbf{M}) = \varepsilon_{ji}(-\mathbf{M}) . \tag{1.54}$$

Applying (1.54) to (1.53), we can immediately see that switching off the magnetic field nulls the off-diagonal elements. Hence, an optically isotropic material becomes optically anisotropic, once it has been magnetized. This is the underlying principle of all MO effects.

The Jones matrix of magnetized samples

Recalling the concept presented in section 1.1, we shall now proceed to defining a Jones matrix of a magnetized sample studied in an optical setup. In the experimental techniques employed in measuring MOKE, the setup is built so that the light beam reflects from the surface of the material. For a demagnetized, optically isotropic and perfectly reflective surface, the Jones matrix is given by (1.25),

$$\mathbf{Z} = \begin{bmatrix} 1 & 0 \\ 0 & -1 \end{bmatrix} .$$

For real samples, however, only a portion of light is reflected a the rest is absorbed or transmitted through the material. Moreover, the reflection generally depends on the polarization of the incoming light (more so in the cases of magnetized samples).

The Jones matrix characterizing these reflective properties can be written as

$$\mathbf{R} = \begin{bmatrix} r_{pp} & r_{ps} \\ r_{sp} & -r_{ss} \end{bmatrix} . \tag{1.55}$$

The indices of the matrix elements correspond to the notation of s- and p-polarization mentioned in section (1.1).

As it was stated in the previous parts, the optical properties of matter, including reflectivity, are completely characterized by the permittivity tensor. We have shown that the symmetry breaking induced by magnetization changes the tensor significantly. It is, therefore, evident that the reflective nature of matter will be modified in the presence of a magnetic field.

[9] One can imagine the magnetic field being produced by an electric loop. Once the time is reversed, the current begins to flow in the opposite direction and the field vector turns to the opposite direction.

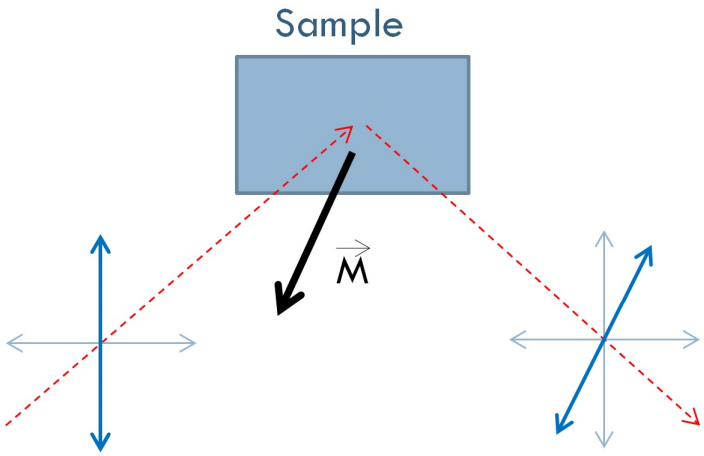

Figure 1.9: A simplified principle of the MO Kerr effect. The magnetization of the samples, $\vec{M}$, changes the polarization of the incident light upon reflection.

This manifests through the elements r_{ij}, as they are, in general, functions of the magnetization vector:

$$r_{ij} = r_{ij}(\mathbf{M})\,. \tag{1.56}$$

The reflection matrix determines the polarization of the reflected beam. Hence, the dependency of its elements on the magnetization vector suggests that the magnetization of the sample will affect the polarization of the probing light (see figure 1.9). This is the so-called magneto-optical Kerr effect (MOKE).

For a general orientation of $\mathbf{M}$, a simple relation between permittivity and the reflection coefficients (1.56) exists only for special configurations - some of which we will discuss later. For now let us only note that these coefficients form a bridge between the material tensors and measurable changes in polarization of the reflected light.

Kerr rotation and Kerr ellipticity

MOKE is characterized by two measurable quantities, Kerr rotation θ_K and Kerr ellipticity ϵ_K (corresponding to change of the azimuth θ and the ellipticity angle ϵ defined in section 1.1). The Kerr effect Φ_K is defined as a complex number,

$$\Phi_K^p := \theta_K^p - i\epsilon_K^p\,, \tag{1.57}$$

$$\Phi_K^s := \theta_K^s - i\epsilon_K^s\,, \tag{1.58}$$

s and p denoting the respective polarizations[10].

The effect itself is determined by the magnetization-dependent ratio of diagonal and off-diagonal elements of the reflection matrix,

$$\Phi_K^p \approx \frac{r_{sp}}{r_{pp}}\,, \tag{1.59}$$

[10]It is important to mention that the sign convention in (1.57) may vary in different books in the same manner as the parameters describing the polarization ellipse (see section 1.1).

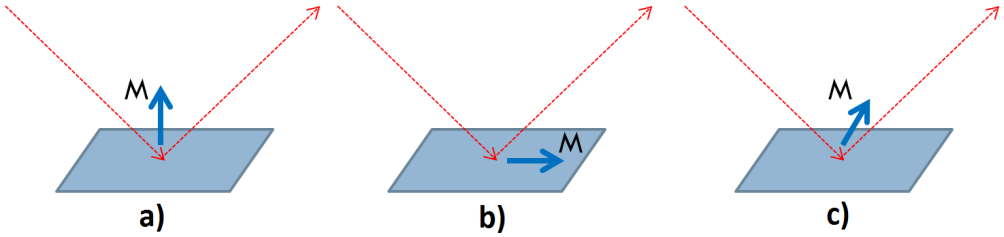

Figure 1.10: Basic MO geometries based on the orientation of the magnetic field and the plane of incidence. a) polar b) longitudinal and c) transversal configuration. **M** denotes the magnetization vector.

$$\Phi_K^s \approx -\frac{r_{ps}}{r_{ss}}\,. \tag{1.60}$$

1.3.2 Polar MOKE

In section 1.2 we have discussed the shape of the permittivity tensor when subjected to a magnetic field directed parallel to the z-axis. Obviously, the permittivity tensor will be in a different form, should the magnetization point in another direction.

Hence, changing the magnetization direction gives different types of MOKE [24]. In magneto-optics, three basic geometries are distinguished (see figure 1.9):

- **Polar** - **M** is parallel to the plane of incidence and perpendicular to sample surface.
- **Longitudinal** - **M** is parallel to the plane of incidence and perpendicular to sample surface.
- **Transversal** - **M** is perpendicular to plane of incidence and parallel to sample surface.

We will now look closely to the geometry used in the experimental measurements employed in this work. For a normal angle of incidence, the matrix (1.55) can be, with the help of (1.59), renormalized as

$$\mathbf{R} = \begin{bmatrix} 1 & -\Phi_K \\ -\Phi_K & -1 \end{bmatrix}. \tag{1.61}$$

Notice that in this case we do not distinguish between Φ_K^s and Φ_K^p, because there is no way of defining a plane of incidence for a normal angle, so s- and p-polarization lose their meaning.

The permittivity tensor for a polar configuration is in the form of (1.53), that has been previously discussed. It is convenient to label its components so that

$$\varepsilon = \begin{bmatrix} \varepsilon_1 & -i\varepsilon_2 & 0 \\ i\varepsilon_2 & \varepsilon_1 & 0 \\ 0 & 0 & \varepsilon_3 \end{bmatrix}, \tag{1.62}$$

which is the convention that we will be using for polar MOKE from now on.

As it is explained in detail in [14], the relation between the tensor and MOKE is, in polar configuration,

$$\Phi_K = \frac{i\varepsilon_2}{\sqrt{\varepsilon_1}(\varepsilon_1 - 1)}\,. \tag{1.63}$$

This is a very important result, as we can now use this relation to gain the spectral dependency of ε_2 through a polar MOKE measurement. However, in order to obtain this dependency, we first need to determine ε_1. That may be achieved by the method of spectroscopic ellipsometry (see section (4.1)).

1.3.3 Linear and quadratic effects

The expansion of permittivity

Let us now discuss the exact dependency of the MOKE on magnetization. The MOKE, in the simplest approximation, has a linear dependency on **M** and for most applications, this is all one has to consider. In reality, however, there are higher-order contributions to MOKE that can manifest themselves in specially designed measurements [25] as well as during routine Kerr analysis, such as measurements of Kerr loops [26].

The permittivity tensor can be expanded in an infinite series[11],

$$\varepsilon(\mathbf{M})_{ij} = \varepsilon_{ij}^{(0)} + \varepsilon_{ij}^{(1)}(\mathbf{M}) + \varepsilon_{ij}^{(2)}(\mathbf{M}) + \dots\,, \tag{1.64}$$

the first element being independent of magnetization [27].

In this work, we shall only confine to studying only the first two of the **M**-dependent contributions, $\varepsilon_{ij}^{(1)}(\mathbf{M})$ and $\varepsilon_{ij}^{(2)}(\mathbf{M})$.

The first-order contribution is the so-called linear magneto-optical Kerr effect (LMOKE) as it only depends linearly on **M**,

$$\varepsilon(\mathbf{M})_{ij}^{(1)} = K_{ijk}M_k\,, \tag{1.65}$$

where we have used the Einstein convention.

The second-order one is called quadratic magneto-optical Kerr effect (QMOKE) and depends on the product of components of the magnetization vector,

$$\varepsilon(\mathbf{M})_{ij}^{(2)} = G_{ijkl}M_kM_l\,. \tag{1.66}$$

Let us now look more closely on the quantities from equations (1.65) and (1.66).

Magneto-optical tensors

K and **G** are the so-called magneto-optical tensors. They govern the MO effects and are closely related to the crystallographic ordering of the material.

[11] The superscript of the respective elements denotes the order of their dependency on **M**.

K is the so-called linear magneto-optical tensor. This third-rank tensor can be represented as a 3x8 matrix [12] when rewriting equation (1.65) as

$$\begin{bmatrix} \varepsilon_{11} \\ \varepsilon_{22} \\ \varepsilon_{33} \\ \varepsilon_{23} \\ \varepsilon_{31} \\ \varepsilon_{12} \\ \varepsilon_{32} \\ \varepsilon_{13} \\ \varepsilon_{21} \end{bmatrix} = \begin{bmatrix} K_{111} & \cdots & K_{113} \\ \vdots & \ddots & \\ K_{211} & & K_{213} \end{bmatrix} \begin{bmatrix} M_1 \\ M_2 \\ M_3 \end{bmatrix} . \tag{1.67}$$

The 24 components of **K** can of course be reduced by using general symmetry relations. For this we find

$$K_{ijk} = K_{jik} \tag{1.68}$$

and

$$K_{iik} = 0 \,, \tag{1.69}$$

for all $i \neq j \neq k$.

As for **G**, this fourth-rank tensor is, for obvious reasons, called a quadratic magneto-optical tensor. In a similar representation, equation (1.66) can be rewritten as

$$\begin{bmatrix} \varepsilon_{11} \\ \varepsilon_{22} \\ \varepsilon_{33} \\ \varepsilon_{23} \\ \varepsilon_{31} \\ \varepsilon_{12} \\ \varepsilon_{32} \\ \varepsilon_{13} \\ \varepsilon_{21} \end{bmatrix} = \begin{bmatrix} G_{1111} & . & . & . & G_{1121} \\ . & . & & & \\ . & & . & & \\ . & & & . & \\ & & & & \\ G_{2111} & & & & G_{2121} \end{bmatrix} \begin{bmatrix} M_1^2 \\ M_2^2 \\ M_3^2 \\ M_2 M_3 \\ M_3 M_1 \\ M_1 M_2 \\ M_3 M_2 \\ M_1 M_3 \\ M_2 M_1 \end{bmatrix} , \tag{1.70}$$

its general symmetry being

$$G_{ijkl} = G_{jikl} = G_{jilk} = G_{ijlk} \,, \tag{1.71}$$

for all $i \neq j \neq k$.

General symmetry relations reduce the number of independent variables per tensor substantially. For a particular crystal structure, this number can be further reduced depending on the symmetry group of the system. The form of MO tensors for all crystal systems can be found in [12] and we will now tend to the simplest one - a cubic lattice.

Cubic crystals

We shall now study the MO tensors for a cubic lattice. In this case, **K** only has six non-zero components, all of them being equal. The linear MO tensor can then be rewritten as

$$K_{cubic} = \begin{bmatrix} K & 0 & 0 \\ 0 & K & 0 \\ 0 & 0 & K \\ -K & 0 & 0 \\ 0 & -K & 0 \\ 0 & 0 & -K \end{bmatrix}, \tag{1.72}$$

which, of course, considerably simplifies equation (1.67).

The quadratic tensor **G** simultaneously breaks down to only three independent parameters denoted as G_{11}, G_{12} and G_{44}. We can rewrite it as follows

$$G_{cubic} = \begin{bmatrix} G_{11} & G_{12} & G_{12} & 0 & 0 & 0 \\ G_{12} & G_{11} & G_{12} & 0 & 0 & 0 \\ G_{12} & G_{12} & G_{11} & 0 & 0 & 0 \\ 0 & 0 & 0 & 2G_{44} & 0 & 0 \\ 0 & 0 & 0 & 0 & 2G_{44} & 0 \\ 0 & 0 & 0 & 0 & 0 & 2G_{44} \end{bmatrix}. \tag{1.73}$$

It is suitable to also write down the zeroth-order element of (1.64) for a cubic crystal. From the part of this work concerning the permittivity tensor for optically isotropic media, it should be evident that

$$\varepsilon_{ij}^{(0)} = \delta_{ij}\varepsilon_1\,, \tag{1.74}$$

where δ_{ij} is the Kronecker delta. The matrix can then be written as

$$\varepsilon_{cubic}^{(0)} = \begin{bmatrix} \varepsilon_1 & 0 & 0 \\ 0 & \varepsilon_1 & 0 \\ 0 & 0 & \varepsilon_1 \end{bmatrix}. \tag{1.75}$$

The MO effects to the second order are, in conclusion, governed by four complex valuables, K, G_{11}, G_{12} and G_{44}. Using present day experimental techniques, K and G_{44} are directly measurable, while for G_{11} and G_{12} we can gain only partial information [25].

2. Heusler compounds

2.1 Basic properties

The Heusler compounds[1] were discovered by a German mining engineer, Friedrich Heusler, in 1903. Heusler studied a 2:1:1 stoichiometric compound, Cu_2MnSn. He found that, although none of its components are magnetic, their compound shows ferromagnetic behavior nonetheless [28].

Since this major discovery, about one thousand of such compounds have been identified. These extraordinary materials are now actively researched due to their application potential in spintronics, magnetic shape memory, superconductors and topological insulators as well as their future utilization in thermoelectronics and solar cells [1].

In this section, we will introduce basic properties of these materials. We will start with their chemical composition and stoichiometry. Next, we will analyze the phenomenon that governs the magnetic properties of these compounds, the so-called half-metallicity (briefly described in the previous chapter). In the third part of this section we will introduce the so-called Slater-Pauling rule. This simple tool is frequently used for calculations of the magnetic moment of Heusler compounds.

2.1.1 Composition

Heusler compounds are generally composed of three elements, here denoted by X, Y and Z. X and Y fall under a group of elements called the transition metals a Z is a main group element (see figure 2.1) [3].

The most recent research has been revolving around cobalt and nickel at the X-position, iron and manganese at the Y-position and silicon, gallium and germanium at the Z-position. detailed information about the material, electronic, optical and magnetic properties of various combinations of these elements are thoroughly summarized in [30]. Recently a group of Heusler compounds with cobalt as the X element has been in the center of attention, having remarkably high Currie temperature [35] and exhibiting an extraordinarily large MO response [25].

The Heusler compounds investigated in this work posses an X_2YZ stoichiometry - these are the so-called full-Heuslers. However, it is possible to prepare Heusler compounds with a different stoichiometry as well. Two other groups of Heusler compounds exist - the half-Heuslers and the inverse Heuslers. The first class is fully stoichiometric, while the other is made with an XY_2Z stoichiometry. For a rather detailed description of the differences between these groups, we recommend the reference [29].

[1] In literature, Heuslers are named "compounds" as often as "alloys", as they technically fall under both of the groups. However, as stated in [1], the term "intermetallic compounds" is the more appropriate one.

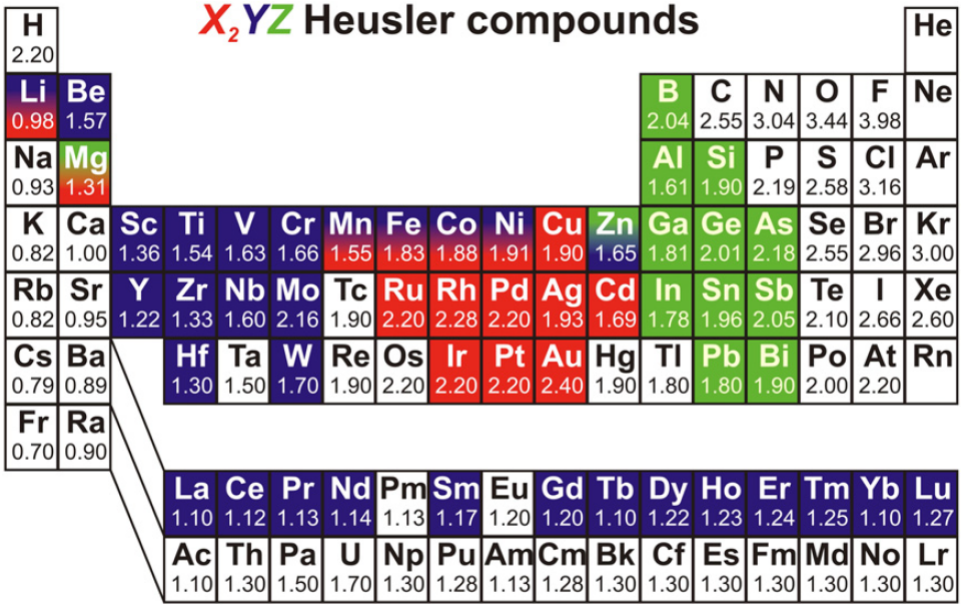

Figure 2.1: The possible composition of the Heusler compounds [1]. X and Y belong in the transition metals (red and blue), whereas the Z element is in the main group (green).

2.1.2 Half-metallicity

One of the many interesting properties of Heusler compounds is the capacity for the so-called half-metallic ferromagnetism. In 1983, de Groot et al. [31] discovered that several Heusler compounds exhibit an asymmetric band character: while some electrons around the Fermi level behave as conduction electrons in metals, electrons with an opposite spin direction experience a band gap as if the material was actually semi-conducting (see figure 2.2).

Let us define the spin polarization P,

$$P = \frac{\rho_\uparrow - \rho_\downarrow}{\rho_\uparrow + \rho_\downarrow}, \tag{2.1}$$

Here $\rho_\uparrow$ and $\rho_\downarrow$ are the spin-resolved densities of states. The arrows $\uparrow$ and $\downarrow$ denote the majority- and the minority-spin states, respectively.

For some half-metallic materials we have a 100% spin polarization around the Fermi level. This feature attracted a large amount of attention due to its potential application in the emerging field of spintronics [22]. The asymmetric character of the energy bands is also responsible for the ferromagnetic properties of Heusler compounds. Thus, the term half-metallic ferromagnetism (HMF) is frequently used. HMF is directly responsible for various interesting spin-dependent phenomena, for instance the anomalous Hall effect ([41]), giant magnetoresistance ([42], [51]) or spin transfer torque [43]. There is a number of other materials capable of HMF. The Heusler compounds are, however, the most suitable ones for future applications due to high Currie temperature [32] and therefore retainability of high spin polarization even at room temperature.

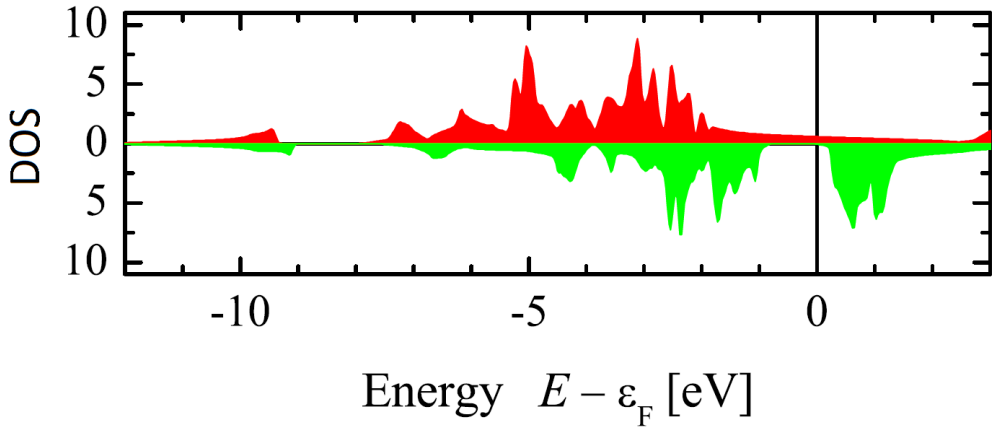

Figure 2.2: The spin-resolved density of states calculated for Co_2FeSi [22]. The green color symbolizes the DOS for the minority-spin carriers, while the red color represents the DOS for the majority-spin ones.

2.1.3 Magnetism

The Heusler compounds may exhibit various magnetic orderings, including ferromagnetic, ferrimagnetic, antiferromagnetic and helimagnetic structures [29]. Their magnetic properties do not depend extensively on the particular elements, but rather on the number of valence electrons N_V [1]. Slater and Pauling (1936 and 1938) have found that the magnitude of the magnetic moment per unit cell, m, can be predicted by a simple rule that has since been called the Slater-Pauling rule:

$$m = N_V - 2n_\downarrow \,, \tag{2.2}$$

Here m is given in multiples of the Bohr magneton, μ_B, and $n_\downarrow$ is the number of electrons in the spin-down states.

The magnetic moment originates from the half-metallic character of the band structure. For fully ordered Heusler compounds, the magnetic moment is caused by the interactions between the X and Y atoms and the consequent hybridization of d-bands. The d-orbitals hybridize due to the position symmetry of the X elements and create five bonding d-states. These states then hybridize with the d-states of Y atoms. This results in 12 occupied minority states, which leads to (2.2) being

$$m = N_V - 24 \,. \tag{2.3}$$

This is the form of the Slater-Pauling rule that is used for the calculation of the magnetic moment of Heusler compounds. If the reader be interested in its detailed derivation, a rather thorough one is presented in [33].

As we can see from (2.3), the magnetic moment is a linear function of the number of valence electrons. We can immediately see that compounds with less than 24 vallence electrons are not magnetic at all.

Let us now present the manifestation of the Slater-Pauling rule in one of the most important groups of Heuslers - the cobalt-based Heusler compounds. In

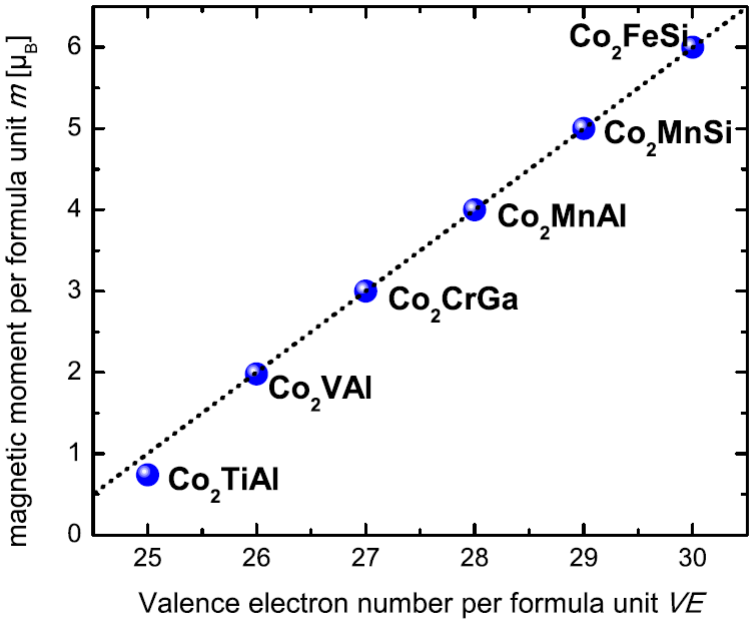

Figure 2.3: The magnetic moment per formula unit as a function of the number of valence electrons per formula unit of the Co-based Heusler compounds [1].

figure 2.3, we present their magnetic moment as a function of the number of valence electrons [1]. As we can see, all of these compounds indeed follow a linear dependency given by equation (2.3).

2.2 Structure

It is a well known fact that the crystallographic ordering influences the properties of all solid-state matter. In the case of Heusler compounds, the crystalline structure affects all of the interesting properties of these compounds, including high Currie temperature and high values of spin polarization. This is why most of the authors investigate the exact structure of the studied samples before proceeding to further analysis.

Here, we will firstly introduce the basic phenomenology used for the description of the crystallographic ordering - the Strukturbericht and Pearson symbolics. Secondly, we will present the ideal Heusler structure, $L2_1$. To achieve this type of structural ordering in the Heusler compounds is a challenging task due to many types of disorder that may arise may arise during the growth process. The disordered phases and their influence on the properties of the compound will be described in the third part of this section. In the last part, we will list the present-day approaches that are used for structure determination. This will later allow us to illustrate the convenience of the usage the MO methods instead.

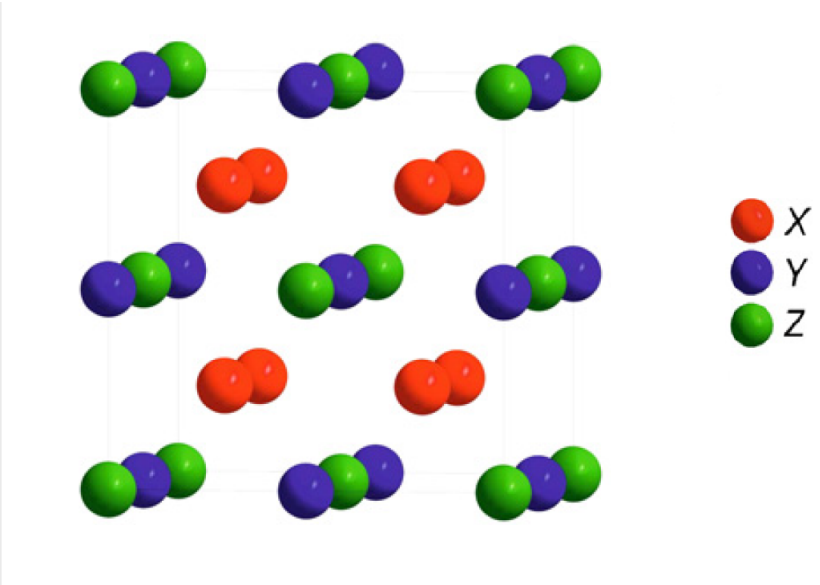

Figure 2.4: The ideal Heusler structure, $L2_1$. The X elements are marked by the red color, Y by the blue color and Z by the green color.

2.2.1 Basic classification

There are several systems used for the description of the crystal structure of solids. The first one is the so-called Strukturbericht notation and the second one is the Pearson symbolism.

The Strukturbericht classification denotes monoatomic crystals X by the letter A, binary crystals XY by B, binary XY_2 by C and so on. After the letter comes a number denoting the specific structure type.

A list of examples is shown in the table bellow.

Material	**Strukturbericht symbol**
Diamond	A4
Graphite	A9
NaCl	B1
CsCl	B2
Perovskite	$E2_1$
Heusler	$L2_1$

Table 2.1: Examples of the Strukturbericht symbolic.

The Pearson (W.B. Pearson) notation involves a lowercase and an uppercase letter, followed by a number. The lowercase letter signifies the particular crystal family - a for anorthic (triclinic), m for monoclinic, o for orthorombic etc. The centering type is denoted by the capital letter - for instance, R stands for rhombohedral centering. Finally, the number simply stands for the number of valence electrons per unit cell.

The materials listed above have the following Pearson symbols:

Detailed information can be found for example in [38].

Although both systems are commonly used for the description of Heusler compounds, in this work we will, for the sake of simplicity, employ the Strukturbericht

Material	Pearson symbol
Diamond	cF8
Graphite	hP4
NaCl	cF8
CsCl	cP2
Perovskite	cP5
Heusler	cF16

Table 2.2: Examples of the Pearson symbolic.

classification only.

2.2.2 Ideal structure

In the ideal case, full-Heusler compounds[2] are formed by four interpenetrating *fcc* sublattices. The X atoms are located at (0,0,0) and (1/2,1/2,1/2) positions, Y at (3/4,3/4,3/4) and Z at (1/4,1/4,1/4) position [36].

Using the Strukturbericht classification, this lattice is denoted by the symbol $L2_1$. This ordering is the cause of the unique properties of Heusler compounds and is generally known as the Cu_2MnAl-type structure, named after one of the compounds discovered by Heusler.

X atoms are positioned tetrahedrally, while Y and Z are organized octahedrally. This composition can be viewed as a zincblende structure (space group $F\bar{4}3m$). Describing the crystallographic ordering in this way is rather convenient as it underlines the covalent bonding between the Y and Z elements. This bonding has a substantial impact on the electronic properties of all Heusler compounds [37].

2.2.3 Disordered phases

Types of ordering

Apart from $L2_1$, there are several other orderings that can be found in Heusler compounds. These orderings has generally negative impact on desired properties of the material (magnetization, spin polarization, etc.) and we will now categorize the most common ones.

Firstly, let us note that all of the bellow-mentioned orderings are viewed as being deviant from the "correct" Heusler structure $L2_1$. Moreover, in all of these arrangements the atoms are positioned in a more random manner than in $L2_1$. Therefore, the term structural disorder is commonly used.

In figure 2.5 we can see various types of disorder that may occur in Heusler compounds. The first type, B2 (CsCl), happens when the Y and Z atoms are distributed evenly in the 4a and 4b positions.

DO_3 (BiF_3), the second type of disorder, is the random swapping of $X \leftrightarrow Y$ or $X \leftrightarrow Z$. This type may be rather challenging to detect using standard X-ray measurements, as will be explained in the last part of this section.

[2]It is important to note that inverse and half-Heuslers crystallize in different orderings with different types of disorder.

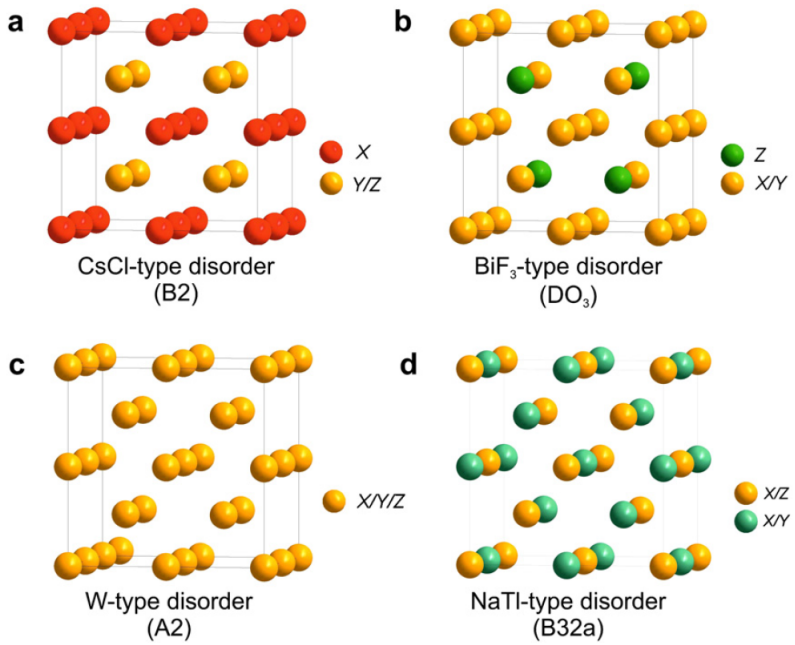

Figure 2.5: The four possible disorders that may arise in the Heusler compounds: a) B2 (CsCl structure) b) $D0_3$(BiF_3 structure) c) A2 (W structure) and d) B32a (NaTl structure) [1].

A rather rare type of disorder, which may often be left out of consideration, is the B32a (NaTl) disorder. The X atoms are located in 8a and Y and Z at 8b positions (randomly).

A completely random distribution of all atoms among all four crystallographic sublattices is called an A2 (W) disorder.

Annealing is the standard method for post-deposit treatment of Heusler compounds. This technique has been reported by many authors to improve the ordering of Heuslers which are usually in an A2-disordered state after the deposition. For temperatures typically around 500^o C the compounds become B2 ordered and start to crystallize in the $L2_1$ phase at temperatures above 700^o C.

The symmetry groups (determined by T. Graf et al. in [1]) and the number of the symmetry operations performable on respective orderings (obtained at [40]) are as follows:

Structure type	**Space group**	**Number**	**Number of operations**
$L2_1$	$Fm\bar{3}m$	225	48
B2	$Pm\bar{3}m$	221	48
$D0_3$	$Fm\bar{3}m$	216	24
B32a	$Fd\bar{3}m$	227	48
A2	$Im\bar{3}m$	229	48

Table 2.3: The symmetry groups of the possible phases in Heusler compounds. The specific space group along with its respective number is followed by the number of the symmetry operations belonging to this group.

Effect on magnetic properties and spin polarization

Disorder from the ideal $L2_1$ structure generally has generally negative impact on the unique spin-dependent properties of Heusler compounds caused by the half-metallic character of their electron structure. Rearranging the atoms in the crystal lattice will, obviously, change the DOS of the material (see figure 2.6). It has been shown by a number of authors that while some disorder may preserve the half-metallicity, other may destroy it completely, blurring the energy gap in the minority-spin DOS. Let us now name several cases of investigation of the impact of disorder on the spin-dependent properties of Heusler compounds.

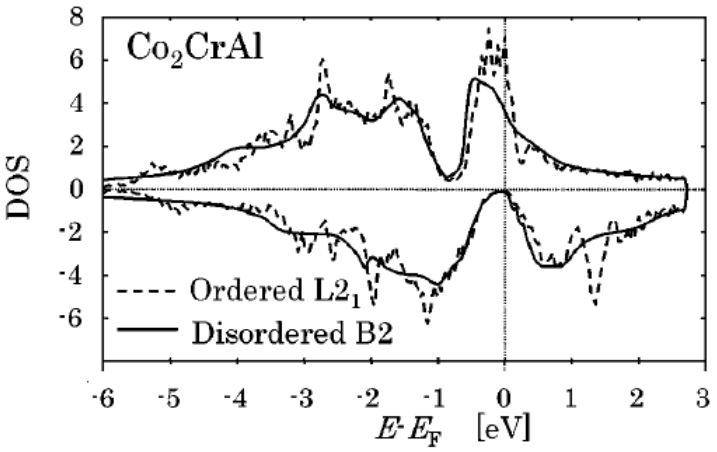

Figure 2.6: The calculated DOS for a perfectly $L2_1$-ordered (dashed line) and a perfectly B2-disordered (full line) Co_2CrAl [46].

For example, Li et al. [44] reported that the DO_3 disorder in $Co_2MnGa_{0.75}Ge_{0.25}$ causes the degradation of spin polarization. In their work Li et al. treated the disorder as anti-site defects between the X, Y and Z elements. They argue that the Co_{Mn} anti-sites (DO_3 disorder) substantially reduce the magnetic moment in the unit cells because the Mn atoms posses spins opposite from the Co atoms.

Similar effect has been predicted for Co_2MnSi in [45]. Using Monte Carlo simulations, Hülsen et al. has shown that the substitution of the Co atom to the Mn or Si site destroys HMF due to the creation of minority spin states in the gap. However, they found that for a fully-ordered $L2_1$ Co_2MnSi Heusler compound the spin polarization is indeed 100% (for T=265 K).

Miura et al. investigated the disorder in Co_2CrAl in [46]. They found that, similarly to Co↔Mn antisites mentioned above, the DO_3 disorder of Co↔Cr considerably decreases the spin polarization (more than 30 % reduction for 90 % ordered structure in comparison to a 100 % ordered one). Miura claims that Cr↔Al (B2) disorder preserves HMF in Co_2CrAl and that the magnetic moment is in accordance with the Slater-Pauling behavior. The spin polarization, however, is reduced only due to the decrease of majority-spin DOS at the Fermi energy.

Aftab et al. [47], which studied the substitution of Cr atoms in Co_2MnSi, has found that while $L2_1$-ordered compounds follow the Slater-Pauling rule (2.3), the presence of A2 disorder causes severe deviations from it. A completely A2-disordered compound shows no magnetic moment whatsoever.

In summary, the order-disorder phenomena has considerable influence on the DOS in the Heusler compounds. As mentioned in chapter 1, the optical methods are an ideal tool for the investigation of these changes. Therefore, using optical probes should enable us to detect structural disorder in Heusler compounds.

Moreover, the results mentioned above prove that the disorder may cause deviation from the Slater-Pauling rule (2.3). This causes a severe change in the magnetic properties of Heuslers and, therefore, their MO properties as well. Thus, a change in structural ordering should be, in principle, detectable by the measurement of MOKE. Before we proceed to this part, let us first name a few methods that are in hand when determining the crystallographic structure of Heusler compounds.

2.2.4 Structure determination

For the reasons that were described in the previous text, the knowledge of the structural ordering in Heusler compounds is of substantial importance. The determination of the exact structure of the compound has become a routine procedure prior to any further investigation.

In this work, we have investigated the Heusler compounds using spectroscopic ellipsometry and MO spectroscopy. There is, however, a number of alternative methods at hand and we will now present the most commonly used ones.

- **X-ray diffraction (XRD)** - One of the most prominent techniques used in crystallography. Viewing the atoms of a crystal as an array of scattering points, XRD uses X-ray radiation to produce secondary electromagnetic waves diffracted by the lattice. The secondary waves interfere negatively in most directions, but there is constructive interference in angles that are typical for particular crystal orderings. These angles are determined by the famous Bragg's law,

  $$2d \sin\theta = n\lambda \,,$$

  where θ is the scattering angle, d is the distance between diffraction planes, n is a positive integer and λ is the wavelength of the X-rays.

  This method, although often used, may not lead to an unambiguous determination of the crystallographic ordering in the case of some of the Heusler compounds. The $L2_1$ ordering and the DO_3 disorder may share the same form-factor (a measure of the scattering amplitude) and their diffraction peaks can therefore completely overlap [1].

- **Extended X-Ray Absorption Fine Structure (EXAFS)** - EXAFS is an oscillating part of the spectrum obtained by X-ray absorption spectroscopy. This method enables the calculation of the X-ray absorption coefficient μ through measuring the incident (I_i) and transparent (I_t) intensities through the relation

  $$\mu = \frac{-\log I_t/I_i}{x} \,,$$

where x is the thickness of the sample.

When plotting the μ spectrum against energy, one observes sharp peaks, each of them corresponding to a ionization state. After every peak, a typical oscillation will occur, originating from the backscattering of waves emitted by the ionized element. This backscattering is caused by the neighboring atoms and are typical for each crystallographic ordering. Basic information can be found in [48].

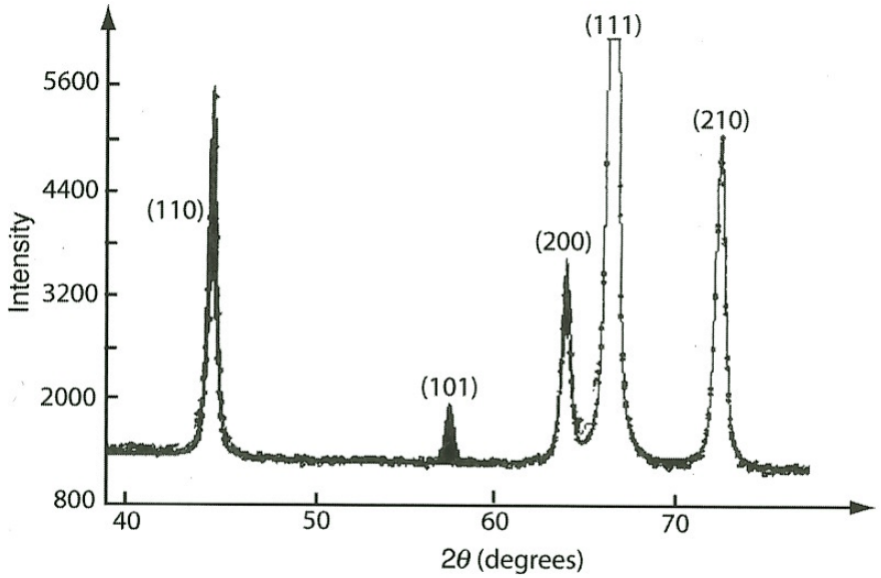

Figure 2.7: An example of the neutron scattering peaks as presented in [49]. The magnetic reflection is shaded.

- **Neutron diffraction** - Suitable for bulk samples, neutron scattering is used in a similar way as XRD. However, unlike X-rays, neutrons interact directly with the atomic cores and, due to their significant energy, can probe further in the sample.

  The neutron scattering is also used for probing the magnetic structure of materials. Although neutrons do not carry any electric charge, they posses a non-zero spin. Neutron diffraction can therefore be used to determine the magnitude and direction of the moments in a unit cell.

  Used neutrons are either thermal or cold (referring to the temperature of the neutron source). They are generated by a nuclear reactor and their energy distribution is narrowed in a crystal monochromator by Bragg's reflection.

  Although a mighty tool for the investigations of the magnetic properties of matter, the necessity for a nuclear reactor remains a considerable disadvantage over other techniques [49].

  Depicted in figure 2.7 is an example of the neutron scattering spectrum.

3. Studied compounds

In this chapter, we will give basic information about the materials that have been investigated in the experimental part of this work. First, we will introduce a new member of the Co-based Heusler compounds - $Co_2FeGa_{0.5}Ge_{0.5}$. We will start with the description of two parental compounds, Co_2FeGa and Co_2FeGe. Next, we will present the characteristics of the compound itself, along with its utilization in present-day spintronic applications.

In the second part, we will present the magnetic-shape memory (MSM) compounds, an extraordinary group of Heusler compounds that has been vividly investigated in the past two decades. Due to the breakthrough of the original magnetic-shape memory compound, Ni_2MnGa, a similar compound of Fe, Mn and Ga has been synthesized. Our research will be focused primarily on this novel material and demonstrating the differences in its characteristics in comparison to Ni_2MnGa.

In this part of the chapter, we shall give a detailed description of both of the compounds as well as a basic introduction to MSM-based technology.

3.1 Ultra-high spin polarization Heusler compounds

3.1.1 Co_2FeGa and Co_2FeGe

Before we proceed to the $Co_2FeGa_{0.5}Ge_{0.5}$, let us first summarize the properties of its two parent compounds, Co_2FeGa and Co_2FeGe. For all spintronic devices, from most the basic (magnetic tunnel junctions) to more advanced ones (second-generation MRAMS, reading heads), a demand for high spin polarization materials is rapidly rising.

The Co-based Heusler compounds, that are known for their half-metallic character and high Currie temperature, have therefore been in the center of attention for many years. In the present days, new Co-based compounds are being developed in order to satisfy the growing demand for high-performance materials.

Since the discovery of the Co_2FeSi Heusler compound, attempts have been made to synthesize a Co_2FeZ compound that would further enhance the properties of the original. Two of the most promising ones were Co_2FeGa and Co_2FeGe.

Co_2FeGa and Co_2FeGe are both half-metallic and while for Co_2FeGe the Fermi energy lies inside the minority-spin gap, for Co_2FeGa it lies outside (see figure 3.1). For both the compounds, the majority-spin electrons at the Fermi energy behave as free carriers.

To set the Fermi energy in the middle of the energy gap of the minority-spin electrons, Co_2FeGa and Co_2FeGe were mixed in an equal amount, creating a quaternary Heusler compound, $Co_2FeGa_{0.5}Ge_{0.5}$. This material has shown some extraordinary results in the very recent past and we will now proceed to their review.

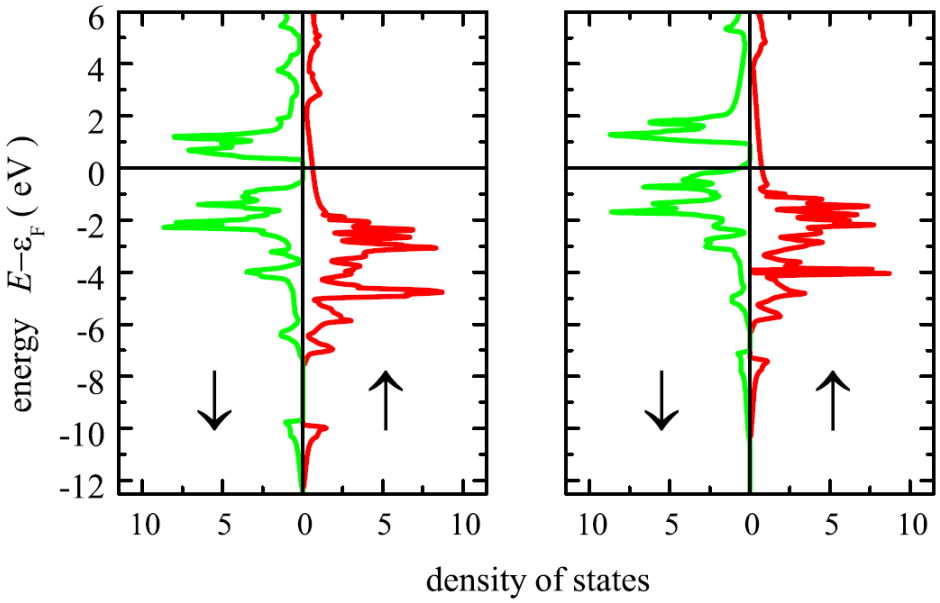

Figure 3.1: The spin-resolved DOS of Co_2FeGe (left) and Co_2FeGa (right) as calculated by Balke et. al. in [22]. The green color symbolizes the DOS of the spin-down states and the red color symbolizes the DOS for the spin-up ones.

3.1.2 $Co_2FeGa_{0.5}Ge_{0.5}$

Since 2013, $Co_2FeGa_{0.5}Ge_{0.5}$ (CFGG) has gained a large amount of attention due to its promising application potential in the current-perpendicular-to-plane giant magnetoresistance (CPP-GMR) devices [51] [52], lateral spin valve-based reading heads [53] and microwave assisted magnetic recording techniques [54].

Out of all Co-based Heusler compounds, CFGG seems to be the most promising one discovered so far. Ikhtiar et al. [53] has shown that its spin polarization is about 15% higher than that of Co_2FeSi or CoFeAl at low temperatures. Moreover, the value of the spin polarization is preserved at room temperature (see figure 3.2), exceeding the spin polarization of Co_2FeSi and CoFeAl by roughly 30%.

As discussed in section 2.2, disorder in Heusler compounds may have a negative impact on the value of their spin polarization. It has been found by Du et. al. [55] that the spin polarization of CFGG is the highest for $L2_1$ ordering and lowers with the increase of B2-disorder. However, even for a B2-disordered structure, the spin polarization is still reasonably high. Due to practical restrictions described in [55], CFGG is usually prepared B2- rather than $L2_1$-ordered. Nevertheless, authors have confirmed that even under such conditions, CFGG is highly applicable in the utilizations listed above.

3.1.3 Research outline

Balke et al. argues that, since the main group element is from the same period of the periodic system as the transition metals, XRD and neutron diffraction cannot unambiguously distinguish between the DO3 and $L2_1$ structures (see section

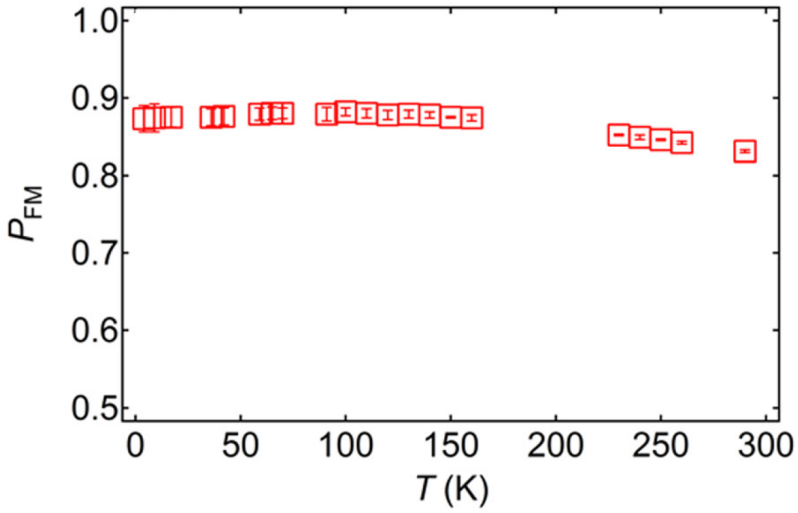

Figure 3.2: The dependency of normalized spin polarization of CFGG on the temperature of the compound as presented in [53].

2.2). In order to determine the quality of the samples, EXAFS and Mössbauer spectroscopy are mostly used.

In section 2.2, we have outlined the basic principle of the above-mentioned methods, as well as their disadvantages. The Mössbauer spectroscopy requires a rather complex experimental setup and the EXAFS spectra may prove to be complicated to interpret.

Therefore, we shall explore the possibilities of an alternative method, the MO spectroscopy, to determine the changes in atomic disorder. MO spectroscopy is a simple, fast and non-destructive method. The setup can be assembled from basic optical components and the spectra do not require any complicated software to be interpreted. Due to these advantages, it may prove to be the perfect tool for the investigation of structural disorder in Heusler compounds.

3.2 Magnetic shape memory alloys

3.2.1 Magnetic shape memory

Since their discovery in 1995, magnetic shape memory compounds (MSMAs) are a subject of wide interest due to their potential application in contactless technology. While devices based upon other active materials are usually operated via electrical contacting, the MSMA technology does not require any wiring, as the active material is operated remotely by magnetic fields. Moreover, in comparison with heat-operated shape memory materials, the MSMAs perform about a hundred times faster.

These assets make the MSMAs a perfect candidate for application as sensors or actuators [2]. Other utilizations include active and passive vibration damping [56]. Simultaneously, new application paradigms such as the MSM contactless microfluidic pump, have also emerged (the basic principle of this pump is depicted in figure 3.3).

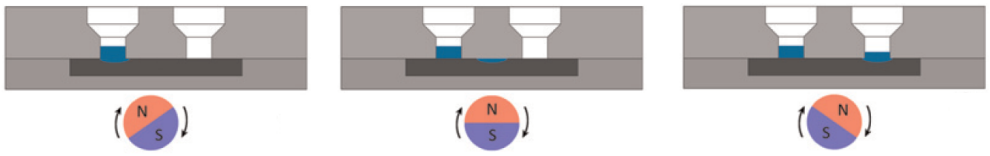

Figure 3.3: The basic principal of a microfluidic pump based on the Ni-Mn-Ga MSM Heusler compound [2]

3.2.2 Fe-Mn-Ga

The first discovered MSM Heusler compound was Ni_2MnGa. Despite the impact it had on the development of the MSM field, Ni_2MnGa cannot be used in the industrial applications due to its limited range of optional temperatures.

Therefore, an intensive search for other MSM materials begun in 1996 in order to further improve the functionality of the MSMAs. Constituents of Ni_2MnGa were replaced by other elements, such as Mn and Co as the Y-element or Al and Ga as the Z-element [57].

In the recent development, the possibility of replacing Ni by Fe at the X-position has been investigated. The Fe-Mn-Ga compounds have been found to exhibit MSM properties as well as Ni_2MnGa (see figure 3.4). Fe-Mn-Ga exhibits a relatively high Currie temperature of up to 750 K and its band structure retains a half-metallic character [58]. The MSM effect may be up to 3.6 % [59].

Regarding their magnetic character, Fe-Mn-Ga compounds were reported to exhibit in ferromagnetic, antiferromagnetic or paramagnetic properties [60]. Their magnetic behavior is, however, quite extraordinary.

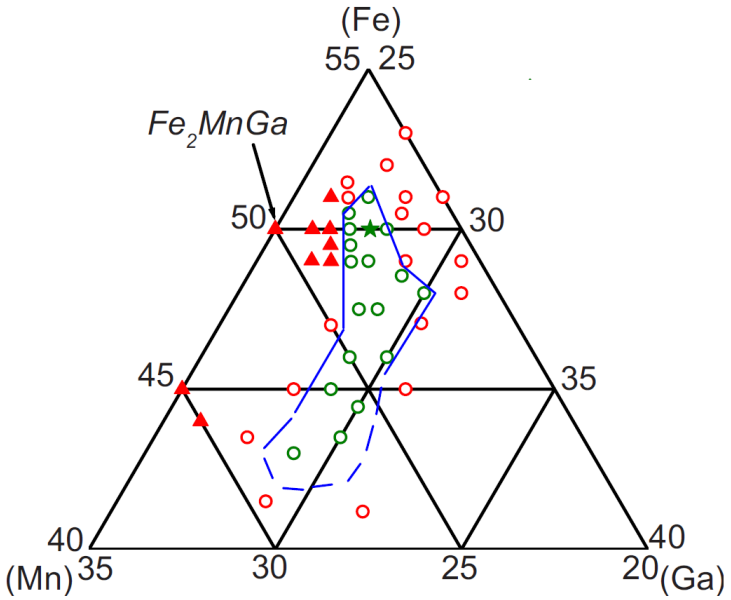

Figure 3.4: The phase diagram of Fe-Mn-Ga compounds. Triangles denote the FCC and BCC structures while the blue line surrounds the compounds that exhibit MSM [59].

An important thermodynamic transition occurs in the Fe-Mn-Ga compounds. For high enough temperatures, Fe_2MnGa is in a paramagnetic austenite phase[1] that is $L2_1$-ordered. At low temperatures, it undergoes a martensite transformation to a ferromagnetic $L1_0$-ordered martensite phase.

As reported by Zhu et al. [59], the martensite phase of Fe-Mn-Ga shows higher magnetization than its parent austenite phase, which is different from the other MSMAs mentioned above, such as Ni_2FeGa, Mn_2NiGa or Ni_2MnAl.

Gasi et al. [58] showed that at room temperature, Fe_2MnGa undergoes a first-order phase transition from a ferromagnetic to an antiferromagnetic phase. Disorder in the material serves as nucleation centers for antiferromagnetic clusters resulting in a coexistence of both phases. As the temperature decreases, the antiferromagnetic inclusions convert to ferromagnetic ones.

Tang et al. [61] reported that the transition from the ferromagnetic to antiferromagnetic phase can be reached in lower temperatures when applying higher magnetic fields - the rate being approximately 10 K/10^3 Oe. Omori et al. [57] have found the same for the martensite transformation from the paramagnetic austenite to the ferromagnetic phase. The temperature increases by 20 K for a field of 7 T.

3.2.3 Ni-Mn-Ga

Similar to Fe-Mn-Ga compounds, at high temperatures Ni_2MnGa exists in a paramagnetic $L2_1$ austenite phase. In temperatures from 350 to 380 K the austenite undergoes a martensitic transformation to a ferromagnetic state.

For perfectly stoichiometric Ni_2MnGa, the magnetic moment is approximately 4.17 μ_B per unit cell. It is primarily localized around the Mn elements as the moment of Mn is approximately 3.5 μ_B.

Recently, a 12% elongation was detected in a nearly stoichiometric Ni_2MnGa compound with small amount of Co and Cu by Sozinov et al. [62]. This is the largest magnetic field-induced reorientation observed up to date.

A major obstacle for large-scale application of Ni_2MnGa compounds is the very limited range of operational temperatures. Ni_2MnGa exhibits magnetic field-induced reorientation up to 300 K. At this point, processes working against the martensitic transformation responsible for the MSM effect begin to occur. Extending the range of operational temperatures has therefore become a contemporary challenge for the MSM research.

A complete summarization of magnetic and mechanical properties, as well as their temperature dependencies can be found in [2] or [63].

3.2.4 Research outline

Exactly how much of Fe should be present in the Fe-Mn-Ga compounds is contemporarily a matter of discussion. Our measurements will be performed on samples with varying amount of iron to determine its effect on optical, magnetic and MO properties. Subsequently, the results will be compared to those obtained for Ni_2MnGa in order to demonstrate the difference between the novel and prototype MSMAs.

[1] Often labeled as being its "parent" phase.

4. Experimental techniques

This chapter is devoted to the description of the experimental techniques used for the investigation of both optical and MO properties of studied samples. It contains description of basic physical principles, which are employed in the measurements, as well as the used equipment.

4.1 Spectroscopic ellipsometry

4.1.1 Basic information

Prior to its description, we should mention that ellipsometry is a rather broad field with a vast number of experimental techniques, setups and utilizations. Here we present only brief summarization of the basic concepts. For more information about this topic, we recommend references [10] or [11].

Spectroscopic ellipsometry is generally defined as the measurement of the change of the polarization state of light either upon reflection or upon transmission and the subsequent analysis of this change based on theoretical modeling. The term "spectroscopic" refers to the fact this change is measured for a continuous spectrum of wavelengths ranging from infrared to ultraviolet light.

This prominent optical method has found use in a vast number of applications. It is mostly employed to determine partial or even complete information about the optical properties of investigated material and sample structure.

The sample structure includes its thickness, surface and interface roughness, composition and conductivity type. The optical properties include the refraction index, permittivity, absorption, reflection and so on.

The change in polarization is traditionally described by the Ψ and Δ parameters. Ψ describes the absolute value of the ratio of reflection coefficients for an s- and p- polarized wave, r_{ss} and r_{pp}, while Δ is their phase shift.

Ψ and Δ are joined into one complex value, ρ, that is commonly defined as

$$\rho = \tan \Psi e^{i\Delta} . \tag{4.1}$$

Ψ and Δ are measured experimentally. Via theoretical modeling and the least square minimization, the spectral dependencies of both real and imaginary parts of permittivity are obtained. These models include the Lorentz and Drude models, described in the first chapter, as well as more advanced theories [11].

4.1.2 Experimental setup

There is a number of possible experimental setups for spectroscopic ellipsometry. The polarizer-analyzer[1] pair is commonly used. The polarizer is used in order to linearly polarize the light emitted by the lamp. The analyzer is used in combination with an intensity detector to analyze the change in polarization of the light reflected from the sample.

[1] "Analyzer" is a term used in such system for a second polarizer. The term originates from its function in the measurement.

The most common ellipsometric setups are based on the so-called null technique. In a PSCA system[2], the polarizer is rotated by and angle α, the compensator by γ and the analyzer by $\beta - \gamma$. Usually, $\gamma = \pm 45^o$ and α and β are set so that the intensity becomes zero at the output [11].

Multiplying the Jones matrices of all optical elements and setting the output intensity to zero, we get

$$\rho = -\tan(\alpha - \frac{\pi}{2}) \frac{\pm 1 + i \tan(\beta - \frac{\pi}{2} \mp \frac{\pi}{4})}{1 \mp i \tan(\beta \mp \frac{\pi}{4})} \,. \tag{4.2}$$

Ψ and Δ are measured for four distinct values of α and β, which excludes the inaccuracy of the estimation of the rotation angles of the polarizer-analyzer pair. The ellipsometric angles are then obtained as

$$\Psi = \frac{1}{4}(\alpha_1 - \alpha_2 + \alpha_3 - \alpha_4) \,, \tag{4.3}$$

$$\Delta = \frac{1}{2}(\beta_1 + \beta_2 + \beta_3 + \beta_4) \,. \tag{4.4}$$

Figure 4.1: RC2 Woolam spectroscopic ellipsometer. The source is located on the right side of the figure, while the detector is located on the left side. The sample holder is situated in the middle.

4.1.3 Equipment

We have used a dual rotating compensator RC2 Woollam ellipsometer (pictured in figure 4.1). It operates in both reflection and transmission modes. The wavelength of the incident light ranges from 190nm (6.5 eV) to 1750 nm (0.7 eV). Hence it covers the near infrared (NIR) region, as well as the visible and the ultra-violet (UV) region.

[2]Polarizer-sample-compensator-analyzer. The ellipsometric setups are usually named in such manner.

To process the experimental data, a rather complex software, CompleteEase, has been used. This tool, developed by J.A. Woollam Co., has been used for the above-mentioned modeling of the optical response of the material.

4.2 Polar MOKE spectroscopy

4.2.1 Basic information

In chapter 1, we explained how measuring MOKE can lead to obtaining valuable information concerning the magnetic properties of materials. As we further discussed in this chapter, MOKE can be measured in three distinct geometries, polar, longitudinal and transversal (see figure 1.10).

In this work, we have measured the spectral dependencies of MOKE in the polar configuration, where the magnetization vector is oriented parallel to the plane of incidence and perpendicular to the surface of the sample. In this geometry, MOKE can be as small as a few millidegrees and the resolution of the setup must be corresponding.

There is a number of methods that can satisfactorily resolve such small changes in polarization and a detailed list can be found in [14]. For spectroscopic measurements, an experimental technique based on rotating analyzer was employed.

4.2.2 The rotating analyzer method

The basic principles of the rotating analyzer method are very similar to those of spectroscopic ellipsometry. The major difference, however, is that the sample is placed in a magnetic field.

The light is emitted by the polychromatic light source L (see figure 4.2). The beam first passes through a linear polarizer P and becomes p- or s-polarized. After propagating through a lens that focuses the beam on the sample S, the light beam is reflected from the sample surface. The reflected beam passes through an analyzer A rotated by an angle α (relative to the crossed position with the input polarizer). The beam is then focused with the help of a second lens and detected by a CCD spectrometer D. Inside the spectrometer, the light is diffracted with the help of a diffraction grating and the intensity at individual wavelengths is detected by a CCD chip.

With the help of this particular setup, the Kerr rotation θ_K is measured. For the measurement of the Kerr ellipticity, ϵ_K, one only has to include a compensator C that changes the phase of the light by δ. This compensator is placed between the sample and the analyzer.

In this geometry, the angle of incidence ϕ should, in principle, be 0^o. In practice, this angle is of course unobtainable [3]. Polar MOKE is, therefore, usually measured for ϕ=5^o or lower.

[3] Although when dealing with monochromatic sources at particular wavelengths, beamspliters can be used in order to obtain it.

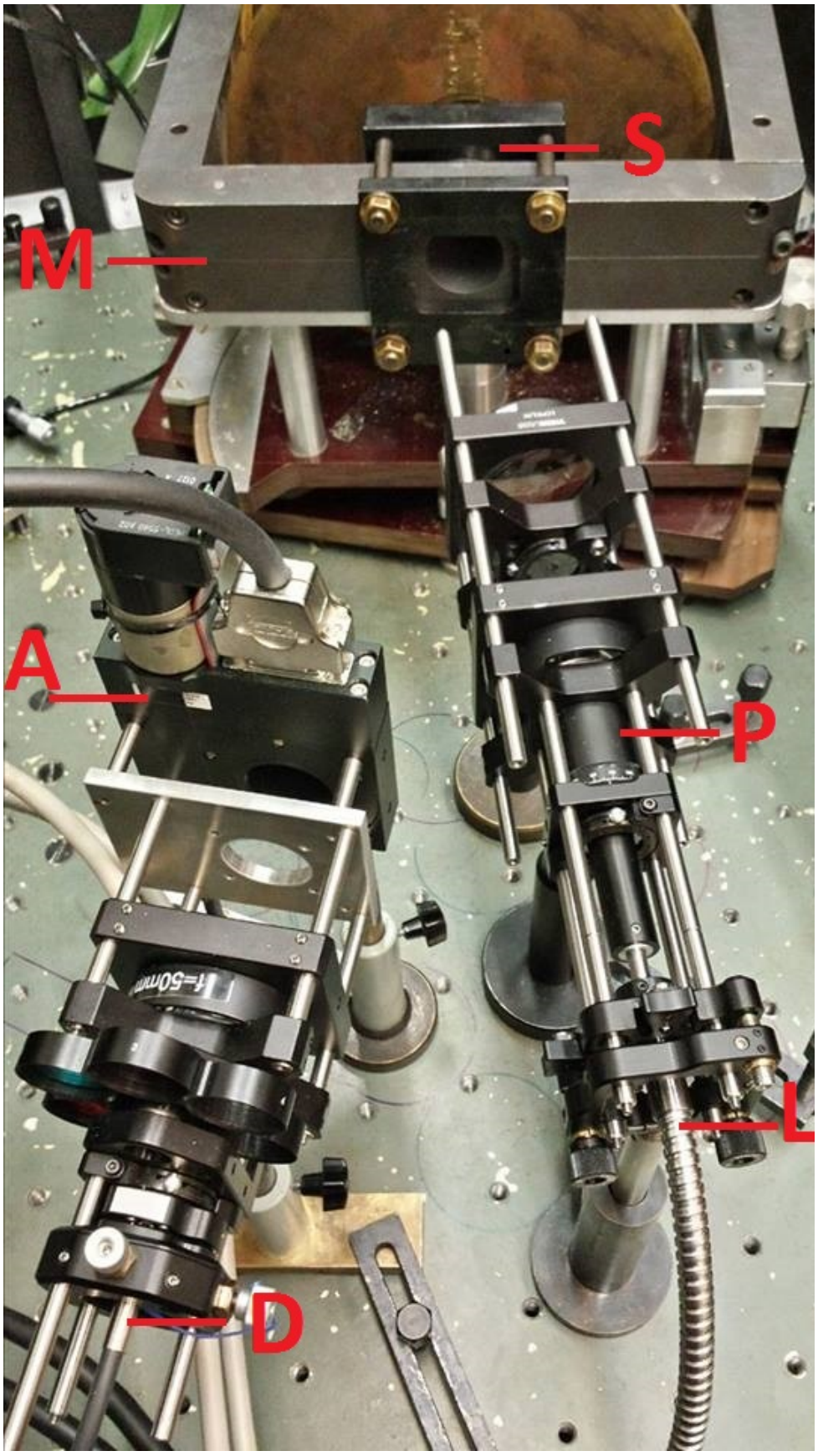

Figure 4.2: The polar MOKE spectrometer. The letter L labels the light source, P the polarizer, A the analyzer and D the detector.

4.2.3 Mathematical description

We shall now proceed to applying the Jones formalism introduced in the first chapter to calculate the output intensity measured by the CCD spectrometer. In the following, we denote the corresponding Jones matrices by the capital letters used for each element in the text above.

Firstly, let us calculate the output polarization state $\mathbf{J_{out}}$ from the Jones vector of the light polarized by polarizer P, $\mathbf{J_{in}}$,

$$\mathbf{J_{out}} = A * C * S * \mathbf{J_{in}} \,. \tag{4.5}$$

By substituting the corresponding Jones matrices we get

$$\mathbf{J_{out}} = \begin{bmatrix} \cos^2\alpha & \cos\alpha\sin\alpha \\ \cos\alpha\sin\alpha & \sin^2\alpha \end{bmatrix} \begin{bmatrix} e^{i\frac{\delta}{2}} & 0 \\ 0 & e^{-i\frac{\delta}{2}} \end{bmatrix} r \begin{bmatrix} 1 & -\Phi_K \\ -\Phi_K & -1 \end{bmatrix} \begin{bmatrix} 0 \\ 1 \end{bmatrix}, \tag{4.6}$$

and, by using standard rules for matrix multiplication,

$$\mathbf{J_{out}} = -r \begin{bmatrix} \theta_K e^{i\frac{\delta}{2}} \cos^2\alpha + e^{-i\frac{\delta}{2}} \sin\alpha\cos\alpha \\ \theta_K e^{i\frac{\delta}{2}} \sin\alpha\cos\alpha + e^{-i\frac{\delta}{2}} \sin^2\alpha \end{bmatrix} . \tag{4.7}$$

Using equation (1.26) we get

$$I_{out} = \frac{1}{2}|r|^2[\cos^2|\theta_K|^2 + \sin^2\alpha + \sin(2\alpha)\Re\{\theta_K e^{i\delta}\}] \,. \tag{4.8}$$

Considering that the Kerr effect is usually in the order of millidegrees, the output intensity is approximately

$$I_{out} = \frac{1}{2}|r|^2[\sin^2\alpha + (\theta_K\cos\delta + \epsilon_K\sin\delta)\sin 2\alpha] \,. \tag{4.9}$$

With no compensator present, I_{out} only depends on the Kerr rotation. Once the rotation is measured, the compensator is added to the setup in order to obtain the Kerr ellipticity as well.

4.2.4 Equipment

The light source used in the measurements was a 150 W Xe lamp made by Hamamatsu Photonics. The spectral range of this lamp is from 185 nm (6.7 eV) to 2000 nm (0.61 eV). The average stability of the lamp is ± 0.5 % per one hour.

P and A were both a-BBO Rochon polarizers. This type of polarizer is made of two birefringent material prisms. Upon entering the second prism, the p-polarized beam continues unchanged in the same direction, while the s-polarized one deviates from it at a wide angle. The second beam is then removed from the setup with the help of an iris-type aperture. The analyzer is set in a rotary stage that rotates with the accuracy of 10^{-3} degree.

The magnetic field is created via a coil electromagnet. Using a 7 A current a 1.4 T field is achieved in polar configuration. The magnet requires water cooling in order to produce stable magnetic field.

We have used a Czerny-Turner-type Andor Shamrock 303i Spectrograph. Its spectral range spans from 190 nm (6.52 eV) to 1100 nm (1.12 eV) with a 0.3 nm resolution. Shamrock 303i uses a blazed diffraction grating to decompose the light and a CCD chip to detect it. The Andor iDus CCD is cooled to -70 ^{o}C using a Peltier cell. This helps to increase the signal-to-noise ratio originating from the dark current.

The light is brought into the setup using a pack of optical fibers with a collimator lens. In the same manner, optical fibers are used to bring the light to the CCD spectrograph.

4.3 Kerr magnetometry

4.3.1 Basic information

Measuring the hysteresis loops is one of the basic tasks encountered when dealing with any magnetic material. From the loop we can deduce the essential magnetic characteristics, ranging from the type of magnetism demonstrated by the material to its coercivity or saturation field.

For this purpose, various methods have been developed. The most common ones are the superconducting quantum interference device (SQUID), the vibrating sample magnetometers (VSA) or inductive sensors.

MO Kerr rotation is, in most cases, linearly dependent on magnetization. Therefore, by changing the magnetic field while simultaneously measuring the Kerr rotation, we can indirectly measure the magnetization of the material. Nowadays, this is perhaps the most common utilization of MOKE measurements.

4.3.2 Differential intensity detection

Let us now briefly introduce another method of measuring MOKE. Unlike the rotating analyzer method, this one is much faster, although not as precise.

The setup again comprises of a light source, polarizer, sample in a polar configuration and a waveplate. In this case, however, the rotating analyzer is replaced by a Wollaston prism W (see figure 4.3).

Wollaston prisms have the ability to decompose light into two orthogonal linear polarizations. The two beams are than detected by a pair of photodiodes.

In addition, a monochromatic source is used rather than a polychromatic one, since the hysteresis loops usually do not differ for various wavelengths. It is convenient to use a wavelength for which the MOKE is the highest, in order to increase the signal-to-noise ratio.

4.3.3 Mathematical description

Similarly to the previous method, we shall now use the Jones calculus to obtain the output intensities, I_1 and I_2. Firstly, $\mathbf{J_{out}}$ is given by

$$\mathbf{J_{out}}^{1,2} = W^{1,2} * C * S * \mathbf{J_{in}} \,. \tag{4.10}$$

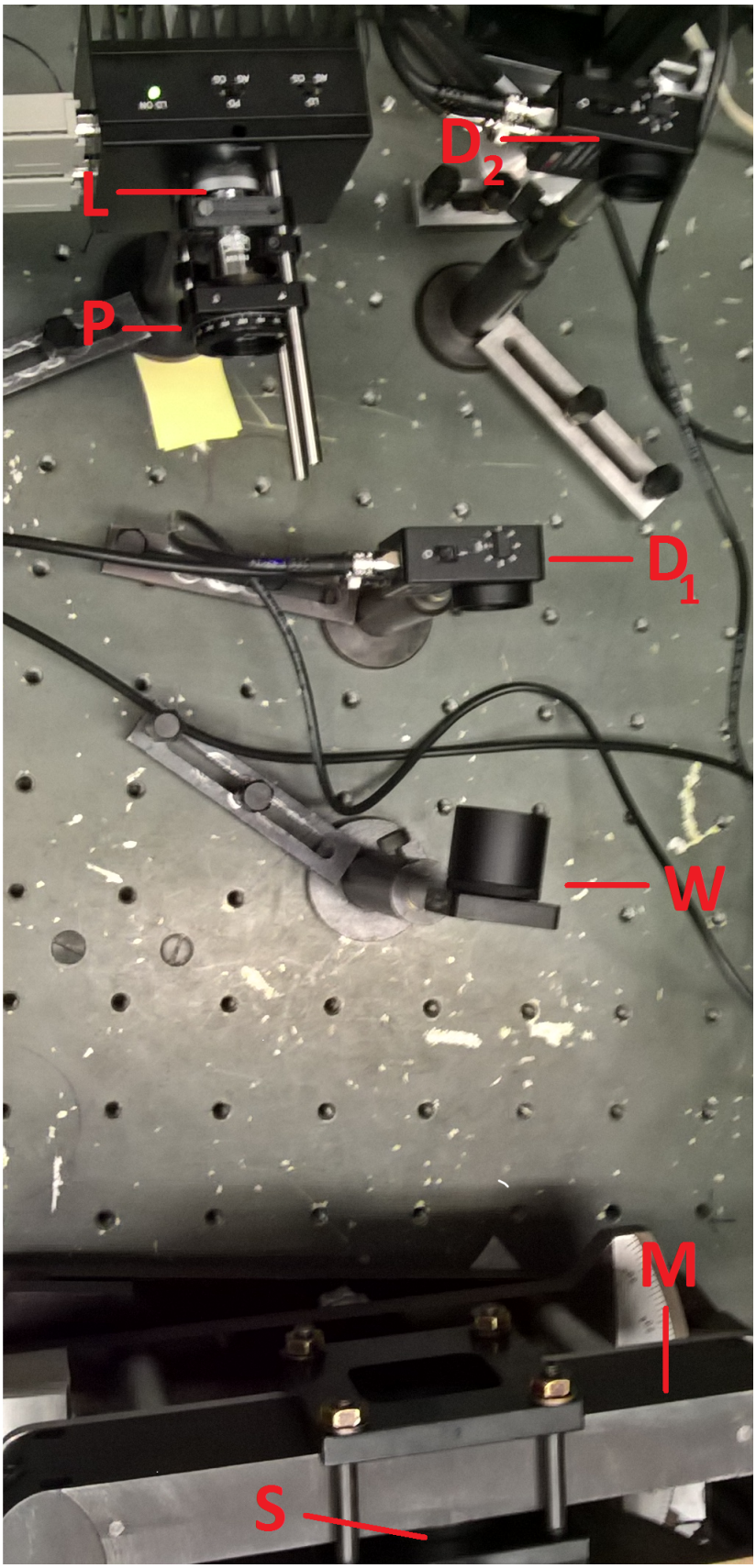

Figure 4.3: The polar Kerr magnetometer. The letter L denotes the laser diode, P the polarizer, S the sample holder, M the electromagnet, W the Wollaston prism and $D_{1,2}$ the photodiodes.

Here $W^{1,2}$ is a Jones matrix that corresponds to the two polarizations $\mathbf{J_{out}}^{1,2}$ [14]. Substituting the respective matrices we obtain

$$\mathbf{J_{out}^{1,2}} = \begin{bmatrix} 1 & \pm 1 \\ \pm 1 & 1 \end{bmatrix} \begin{bmatrix} e^{i\frac{\delta}{2}} & 0 \\ 0 & e^{-i\frac{\delta}{2}} \end{bmatrix} \frac{r}{2} \begin{bmatrix} 1 & -\Phi_K \\ -\Phi_K & -1 \end{bmatrix} \begin{bmatrix} \cos\alpha \\ \sin\alpha \end{bmatrix}, \tag{4.11}$$

where α is a very narrow angle by which the polarizer is rotated with respect to the s-polarization.

Consequently, using equation (1.26), we get

$$I_1 - I_2 = |r|^2[\epsilon_K \sin\delta - (\theta_K + \alpha)\cos\delta]\,. \tag{4.12}$$

Using (4.12) we can gain the values of the MO angles. For the measurements of hysteresis loops, only the Kerr rotation is predominantly measured. Therefore, the waveplates can be excluded from the setup completely.

4.3.4 Equipment

Except for the detectors and light source, the setup has been build with the same equipment as the previous one.

We have used standard laser diodes made by Thorlabs with a wavelength corresponding to the highest MOKE exhibited by the particular sample. The beams were detected by PDA100A Si amplified photodiodes made again by Thorlabs. Their spectral sensitivity was between 320 nm (3.87 eV) and 1100 nm (1.12 eV).

The magnetic field has been varied between -1.4 an 1.4 T. The field was measured first in situ via a Hall probe and then remeasured with no sample present in order to obtain the exact value of the magnetic field in the sample location.

5. Experimental results

The previous chapters contained both theoretical and experimental approaches to the research of Heusler compounds. We have also added the basic information about two extraordinary members of the Heusler family - $Co_2FeGa_{0.5}Ge_{0.5}$ and Fe_2MnGa. In this chapter we will provide the results obtained for these two materials by the tools presented in the previous text.

Starting with $Co_2FeGa_{0.5}Ge_{0.5}$, we will first summarize the basic characterization given by E. Vilanova, the author of the $Co_2FeGa_{0.5}Ge_{0.5}$ samples studied in this work. This includes X-ray diffraction and atomic force microscopy measurements. We will continue by presenting our own research, namely the results of spectroscopic ellipsometry, MO spectroscopy and MO magnetometry. To confirm our interpretation of the experimental results, ab initio calculations made by Dr. Kudrnovsky will also be presented in this part.

In the second part, we will present the results obtained for Fe_2MnGa. This section will only contain our original results, again obtained by spectroscopic ellipsometry, MO spectroscopy and MO magnetometry. Those will be compared to the results we have obtained for Ni_2MnGa, for reasons that were explained in section 3.2.

5.1 $Co_2FeGa_{0.5}Ge_{0.5}$

5.1.1 Sample description

A set of sixteen $Co_2FeGa_{0.5}Ge_{0.5}$ (CFGG) samples was made by E. Vilanova at the Johannes Gutenberg University of Mainz [64]. The samples were deposited using an ultrahigh vacuum DC-sputtering system.

During the deposition process, the chamber was first outgassed to the pressure of roughly 10^{-9} mbar. The system was then filled with inert high purity Ar gas. The pressure in the chamber has been set to approximately 10^{-2} mbar.

The CFGG compounds were sputtered on (100) MgO substrate. This substrate is commonly used for Heusler compounds as it reportedly allows high quality epitaxial growth. Heusler compounds generally grow diagonally on MgO, e.i. rotated by 45^o with respect to the cubic structure of the substrate.

The samples differ in both thickness and deposition temperature. The substrate was heated to temperatures between 650 and 1050^o C. For each sample, the corresponding deposition temperatures are listed in table 5.1. The thickness of the samples ranges from 15 to 80 nm and was estimated by XRR in [64]. After the deposition, all samples were caped by several nanometers thick Pt layer.

5.1.2 Atomic force microscopy

In order to obtain surface roughness of the CFGG samples, a series of atomic force microscopy (AFM) and topography measurements was performed [64]. For samples deposited at temperatures around 650 ^{o}C, the surface creates a labyrinth-like structure, while the estimated roughness is approximately 15 nm.

Number	**Deposition temperature** [^{o}C]	**Thickness** [nm]
68	1050	83
69	1050	Unknown
70	1050	33
56	950	67
57	950	52
58	950	24
59	850	62
60	850	34
61	850	24
62	750	55
72	750	71
63	750	41
64	750	23
73	750	21
65	650	53
66	650	33
71	650	20

Table 5.1: Parameters of the CFGG sample set (evaluated by Vilanova [64])

However, when increasing the deposition temperature to 750 ^{o}C, CFGG starts to form columns separated by cave-like cavities (see figure 5.1a). These cavities begin to fall down to the MgO substrate for temperatures above 950 ^{o}C.

The height of the columns is determined not only by the deposition temperature of the samples, but also by their thickness. As it is shown in figure 5.1b, the roughness of the samples increases with the CFGG layer thickness.

The creation of the column-like surface in CFGG thin films deposited at high temperatures was also reported by Li et. al. [51]. Using AFM, Li investigated film stacks of annealed CFGG-Ag-CFGG deposited on Cr-Ag buffer layers grown on a (001) MgO substrate. It was found that for these samples, the cracks begin to form at the annealing temperature of 650^o C.

5.1.3 X-ray diffraction

In order to study the structural disorder of the compounds, X-ray diffractometry (XRD) measurements were performed by Cejpek and Vilanova [64]. As it has been mentioned in the previous chapter, the order-disorder phenomenon is hard to detect unambiguously by XRD in the case of some Heusler compounds.

The DO_3 disorder in CFGG is the random exchange of Co and Fe atoms in an $L2_1$ Heusler lattice. These atoms, however, share the same form factor. Hence, both orderings provide a non-vanishing (111) peak in the XRD spectrum.

The intensity of the (111) diffraction peak is, however, lowered by the presence of B2 disorder. Therefore, by measuring the height of the (111) diffraction peak we are able to determine the change of the amount of the B2 disorder in the CFGG compounds.

The amount of A2 disorder can be estimated from the height of the (200) peak, which vanishes for a perfectly A2-disordered compound. In addition, the

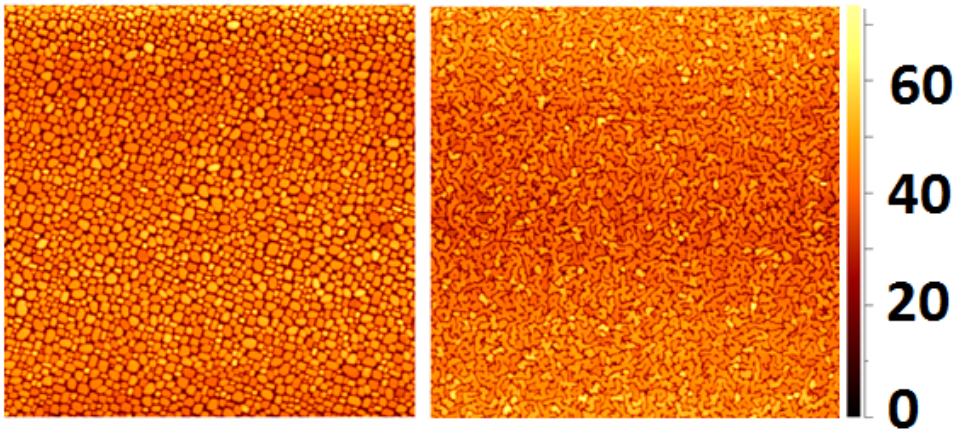

(a) Left: sample no. 68 (T_d=1050^o C, 80 nm thick). Right: sample no. 62 (T_d=750^o C, 53 nm thick).

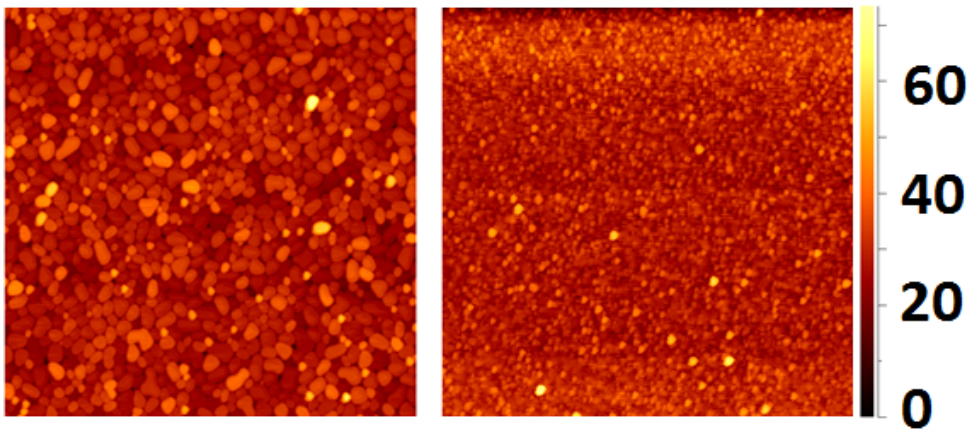

(b) Left: sample no. 56 (T_d=950^o C, 66 nm thick). Right: sample no. 58 (T_d=950^o C, 24 nm thick).

Figure 5.1: Comparison of AFM results for CFGG [64]. a) Samples varying by temperature, b) samples varying by thickness.

(111) peak also lowers by the presence of the A2 phase.

In summary, by measuring the ratio of the peak intensities I_{111} and I_{200}, one can determine the change in the ratio of $L2_1$, B2 and A2 disorders present in the CFGG samples. The results are, however, influenced by the DO_3 disorder as it also contributes to I_{111}.

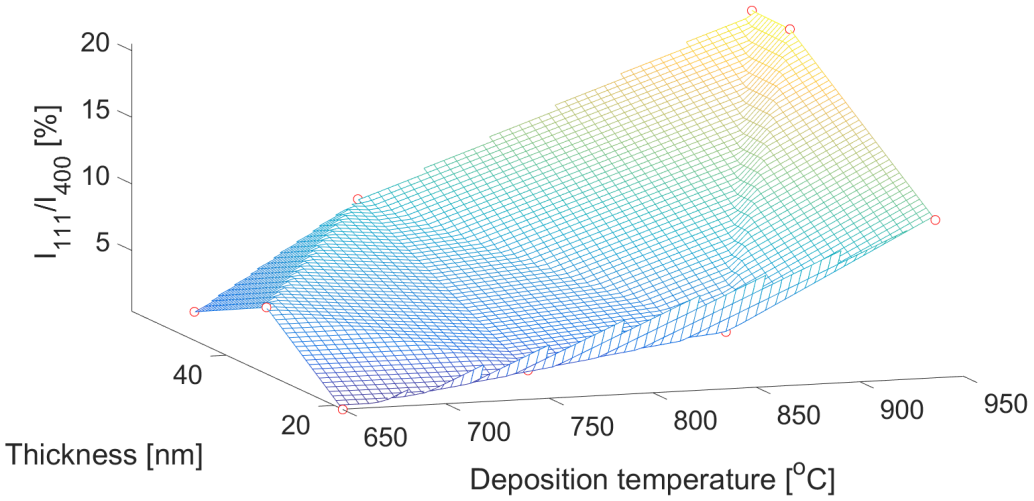

Figure 5.2: Results of XRD measurements performed by Petr Cejpek. The x-axis represents the deposition temperature, y-axis the thickness of each sample. On the z-axis there is the ratio of I_{111} and I_{400} which represents the content of the $L2_1$ and DO_3 phases present in the samples divided by the content of the B2 phase.

Using the information given above, Vilanova [64] has found that the ratio of I_{111} and I_{200} gradually rises with the deposition temperature and reaches a maximum at 650^o C. Ab initio calculations show that the DO_3 has a relatively high formation energy. According to Vilanova, it becomes considerable at temperatures higher than 600^o C. Therefore, XRD measurements will not provide the precise amount of the $L2_1$ phase present in the CFGG compounds for the samples investigated in this work.

In figure 5.2 we present results of XRD scans obtained by P. Cejpek. As we can see, the overall amount of $L2_1$ and DO_3 phases rises with the deposition temperature at the expense of the B2 disorder.

From the XRD results it can also be seen that the amount of $L2_1$ and DO_3 phases is slightly lower for thinner samples. However, an opposite trend has been observed in [64] for samples deposited at temperatures between 490 ^{o}C and 710 ^{o}C. In figure 5.3 we see a gradual decline of this ratio for lower deposition temperatures and thicker samples.

Figures 5.2 and 5.3 give a partial image of the creation of structural disorder in CFGG thin film samples varying by both deposition temperature and thickness. When rising the deposition temperature from 450^o C, the amount of the $L2_1$ phase increases, which manifests itself in the increase of the I_{111} peak. It has been shown by Li et. al. [51] that this is at the expense of the A2 phase, as the amount of B2 disorder remains almost constant at this temperature range. This confirms the well-known fact that the A2 disorder can be suppressed by this kind of temperature treatment.

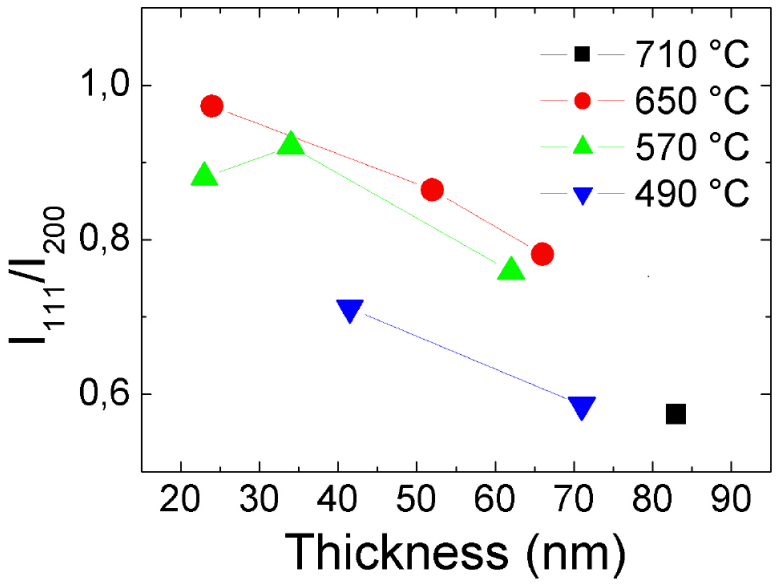

Figure 5.3: Results of XRD measurements performed by Enrique Vilanova [64]. The x-axis represents sample thickness and the y-axis the amount of the $L2_1$ and DO_3 phases present in the samples divided by the amount of the B2 phase.

From the figures above we can see that the I_{111}/I_{200} ratio lowers with the thickness of the samples deposited at the temperature range between 490 and 710 ^{o}C. Above 650 ^{o}C the possibility of the creation of the DO_3 disorder may occur. At this point, it cannot be unambiguously distinguished from the XRD spectra, whether the rise of the I_{111}/I_{200} ratio is caused by $L2_1$ or DO_3. A series of optical and magneto-optical measurements was therefore conducted in order to investigate CFGG thin films deposited at this temperature range.

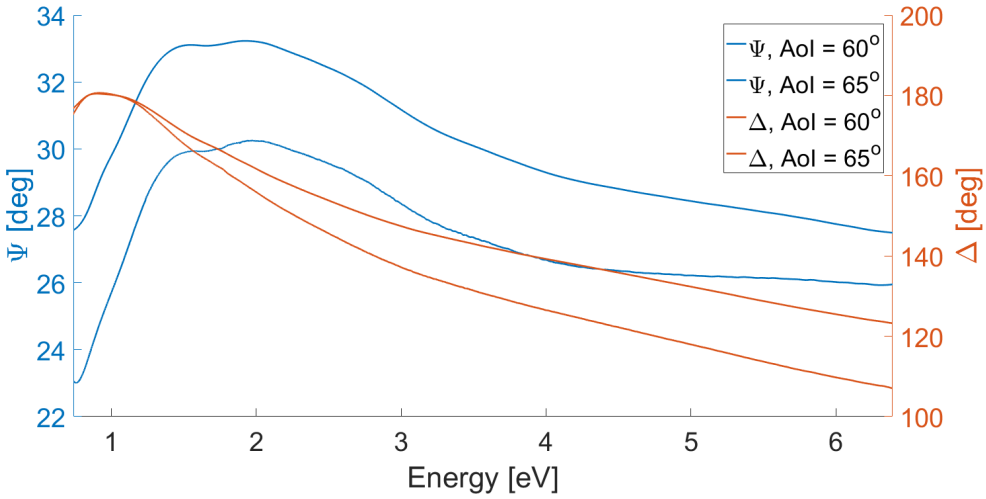

Figure 5.4: An example of the Ψ (red lines) and Δ (green lines) spectra measured in reflection mode at the angles of incidence (AoI) of 60^o and 65^o. The results are shown for the sample number 60 (T_d=850 ^{o}C, 34 nm thick).

5.1.4 Spectroscopic ellipsometry

As it was explained in the previous part, the XRD results cannot be unambiguously interpreted. In order to determine the exact amount of the $L2_1$ phase present in the samples, we examined the electron structure of the materials by the means of spectroscopic ellipsometry. This technique, together with the particular method and equipment used in this work, is described in section 4.1.

Before the measurements, the samples were cleaned using high-purity ethanol for UV spectroscopy. The spectra of Ψ and Δ were measured for each of the CFGG samples. These spectra were measured at three different angles of incidence, 55^o, 60^o and 65^o in the photon energy range from 1.24 to 6.5 eV. An example of the Ψ and Δ spectra is shown at 5.4.

As explained in section 4.1, the most important part of the spectroscopic ellipsometry routine is the theoretical fitting of the data that were obtained experimentally. Our model describes the samples as a thin layer of CFGG on an MgO substrate. Above the CFGG compound there is another layer, described by the effective medium approximation[1] (EMA). This layer contains a mixture of air, Pt and CFGG and represents the surface roughness of the samples.

The thicknesses together with the optical properties were fitted via the least square method. The starting points of these fits are the corresponding thicknesses measured by XRR. The ratio of the constituents in the EMA layer was fitted as well.

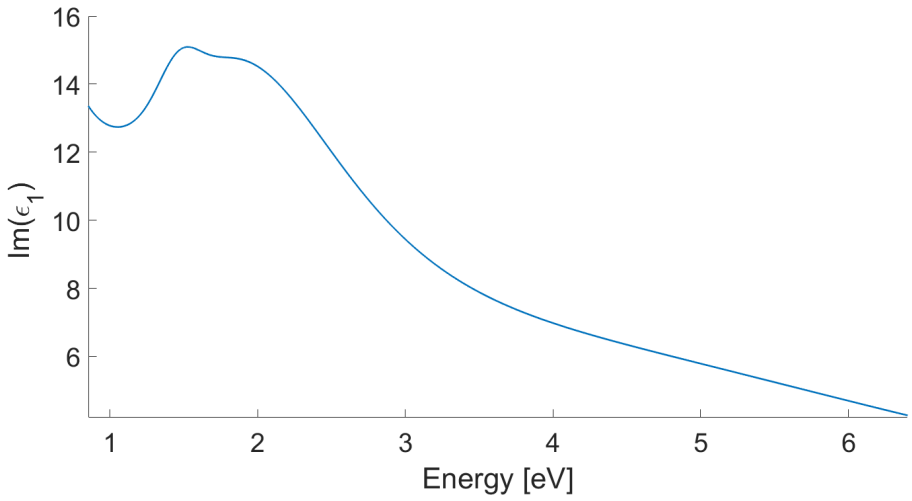

Figure 5.5: An example of the spectral dependence of ε_1. The results are shown for the sample number 61 (T_d=850 ^{o}C, 24 nm thick).

An example of the spectrum of the diagonal part of the permittivity tensor (its imaginary part) can be found in figure 5.5. In the NIR part of the spectrum the optical response begins to rise in a Drude-like manner (see section 1.2). In figure 3.1, we can see a non-zero DOS for the majority states around the Fermi energy. These states describe free electrons that behave as in metal, hence contributing to the permittivity spectrum in a way that can be described by the Drude model.

Between approximately 1.5 and 2.5 eV we can see two peaks. These correspond to the distance between the states on both sides of the gap in the minority-spin

[1]Bruggeman model.

DOS (see again figure 3.1). The minority-spin electrons around the Fermi energy behave as if they were in a semi-conducting medium, their contribution to the optical response can therefore be characterized by the Lorentz model.

For each CFGG sample, we have measured the Ψ and Δ spectra and calculated the spectral dependence of both real and imaginary parts of ε_1 using the model described above.

The resulting spectra of both real and imaginary part of permittivity are displayed in figures 5.6 and 5.7.

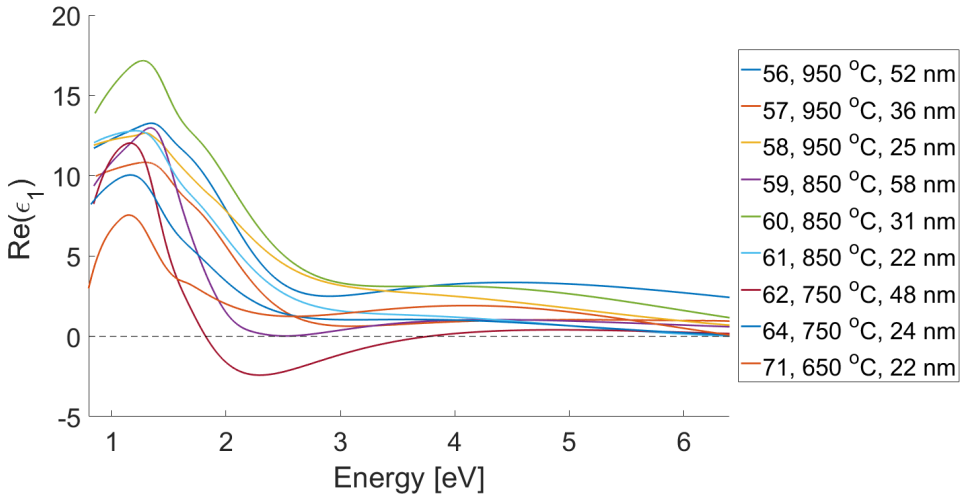

Figure 5.6: The spectral dependence of the real part of ε_1 of the CFGG samples 56 through 71. The legend contains the number of the sample, its deposition temperature and thickness calculated by theoretical modeling of the optical response.

Since the electronic structure of materials is directly connected to the imaginary part of permittivity (see section 1.2), the real part was further left out from our considerations and only the imaginary part will be discussed.

We will now focus our attention on the Lorentzian transitions mentioned above. From figure 5.7 we can see that the lower-energy peak slightly shifts to higher energies as the deposition temperature rises.

This dependency is more evident in figure 5.8. We have extracted the energy of the Lorentzian transition from the ellipsometric data and plotted their dependence on the thickness and deposition temperature of the respective samples.

We can clearly see that the electron transition moves to higher energies for samples with higher deposition temperatures. For samples with thickness around 23 nm this change is approximately 0.5 eV, that is almost 30% of the low-temperature value. We can also see a slight decrease of the transition energy for thicker samples.

5.1.5 Magneto-optical spectroscopy

As it has been mentioned in section 2.2, the disorder in Heusler compounds has a substantial impact on their electric, magnetic and optical properties. The disorder generally changes the magnetic moment of the Heusler structure and should,

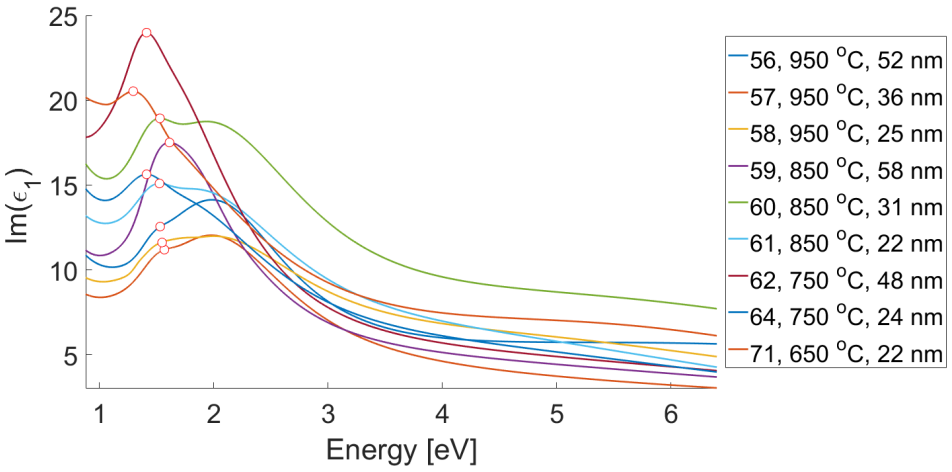

Figure 5.7: The spectral dependence of the imaginary part of ε_1 of the CFGG samples 56 through 71. The legend contains the number of the sample, its deposition temperature and thickness calculated from the optical response. The red circles represent the maxima of the lower-energy Lorentzian peaks.

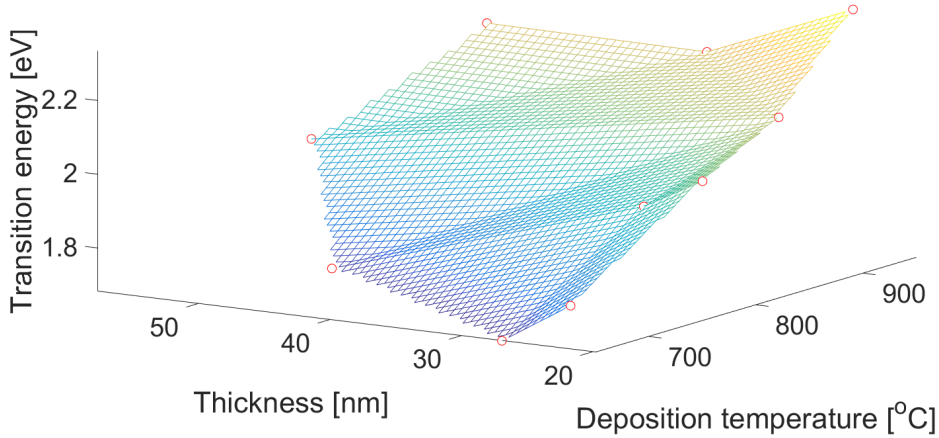

Figure 5.8: The energy of the low-energy Lorentzian peak as a function of the deposition temperature and thickness of the CFGG samples. The red circles represent the width of the energy gap obtained from the analysis of the Im$\{\varepsilon_1\}$.

therefore influence its magneto-optical response. In addition, the ellipsometric results have shown a shift in the electronic transition energies for high-temperature samples. This should also affect the measured MO response via linear MO tensor (see section 1.3).

We have measured the spectrally dependent Kerr rotation θ_K and Kerr ellipticity ϵ_K for each CFGG sample. The spectra were measured in polar configuration using the method presented in 4.2. In figures 5.9 and 5.10 we present examples of the Kerr rotation and Kerr ellipticity spectra (sample 64).

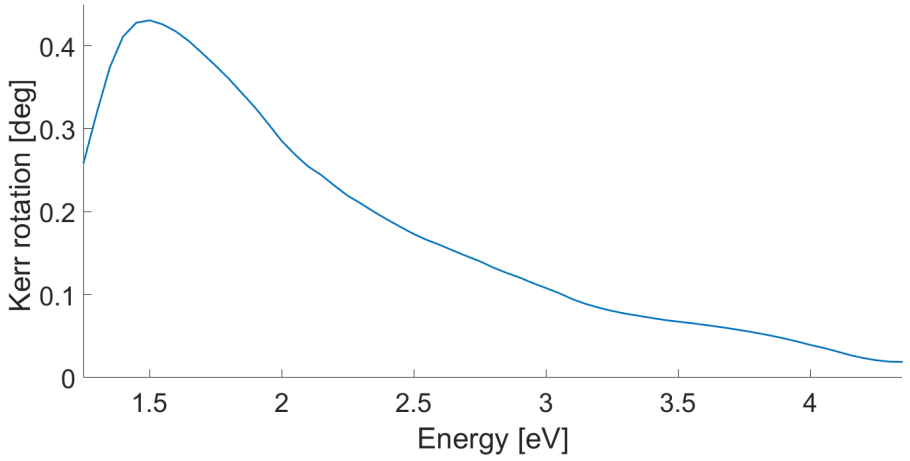

Figure 5.9: The Kerr rotation spectrum for the sample number 64 (T_d=750 ^{o}C, thickness 23 nm).

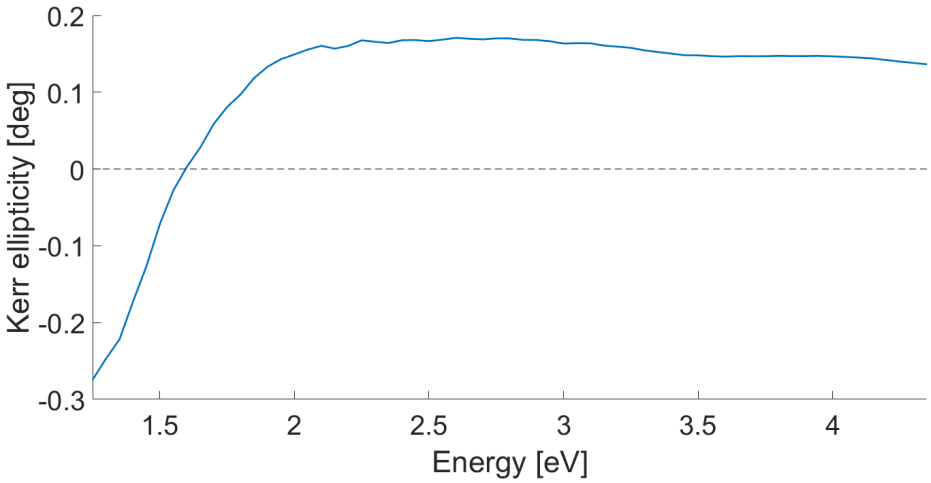

Figure 5.10: The Kerr ellipticity spectrum for the sample number 64 (T_d=750 ^{o}C, thickness 23 nm).

Let us now focus our attention on the Kerr rotation spectrum. We can see a large (over 0.4 degrees) peak rising near 1.5 eV. The Kerr rotation slowly drops for higher energies, becoming almost negligible in the UV region.

The Kerr ellipticity, on the other hand, remains almost constant over the visible and UV regions and exhibits a rise in amplitude in the NIR part of the spectrum.

The measured Kerr spectra for each CFGG sample are presented in figures 5.11 and 5.12. We can see that all of the samples exhibit a similar MO response, sharing a rotation peak in the NIR region.

In order to analyze the MO response further, we have, in the same manner as with the ellipsometry results, investigated the NIR peak in the Kerr rotation spectra. The respective maxima of Kerr rotation are denoted by a red circle in figure 5.11.

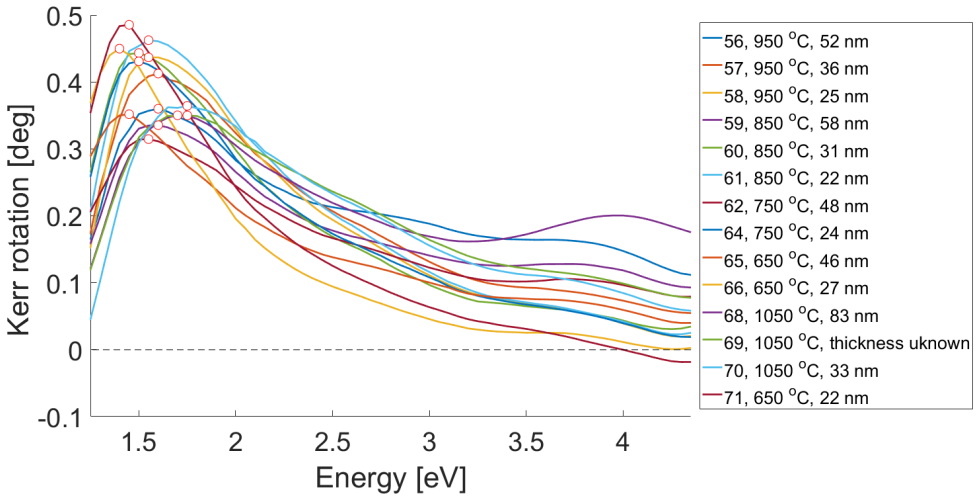

Figure 5.11: The Kerr rotation spectra for all CFGG samples. The legend contains the deposition temperature and thickness for each sample. The maximum Kerr rotation for each sample is denoted by a red circle.

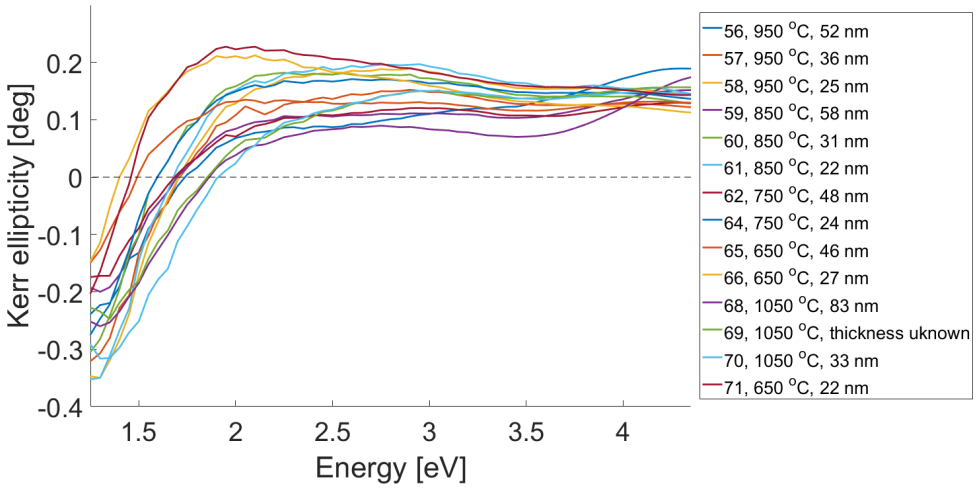

Figure 5.12: The Kerr ellipticity spectra for all CFGG samples. The legend contains the deposition temperature and thickness for each sample.

To illustrate the behavior of the peak, we present the maximum of the Kerr rotation with respect to the thickness and deposition temperature of the sample in figure 5.13.

The amplitude of the peak decreases for high deposition temperatures and thick samples. The maximal Kerr rotation decreases roughly by 0.13 degrees for

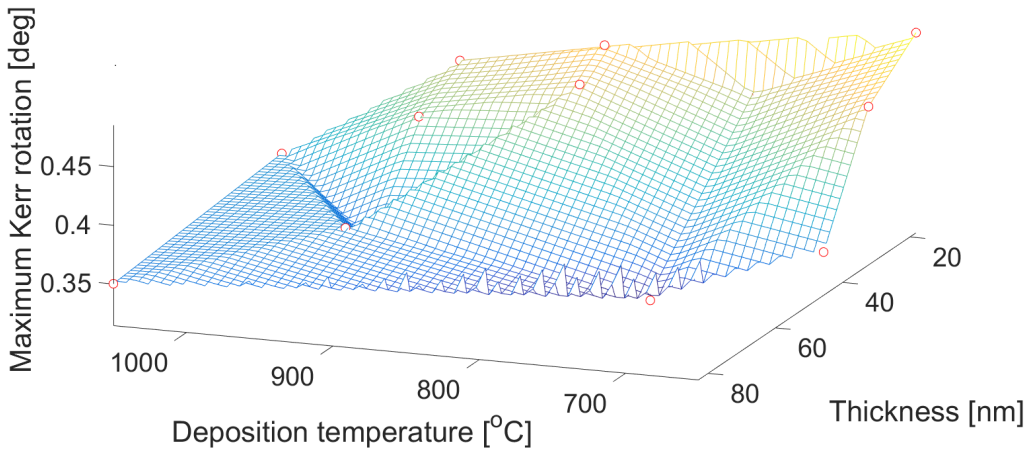

Figure 5.13: The maximum Kerr rotation as a function of thickness and temperature of the CFGG samples.

the samples with the highest deposition temperature and highest thickness.

Finally, we have combined the spectra obtained by spectroscopic ellipsometry with the Kerr spectra presented in this section and calculated the off-diagonal part of permittivity for each sample. In figures 5.14 and 5.15, we present the calculated spectra of the real and imaginary parts respectively.

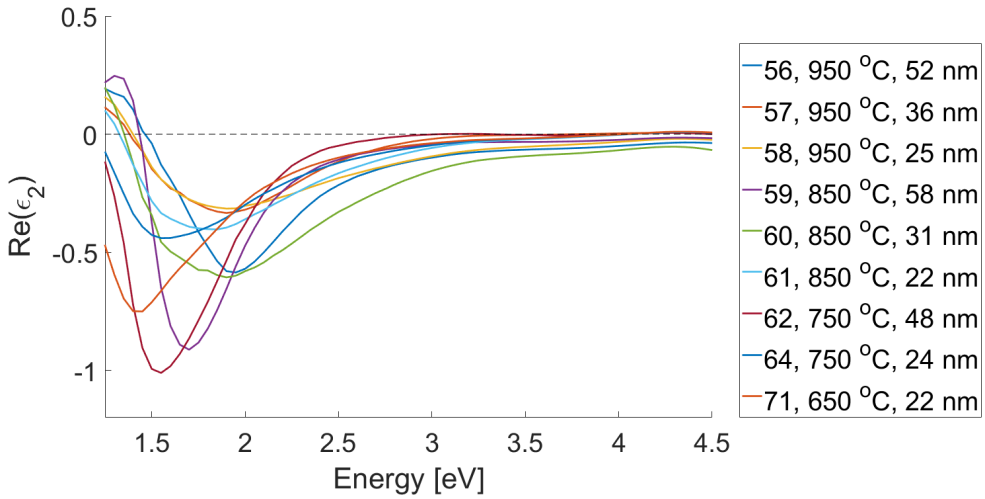

Figure 5.14: The spectral dependence of the real part of ε_2 of the CFGG samples 56 through 71. The legend contains the number of the sample, its deposition temperature and thickness calculated from the optical response.

In figure 5.15, we have marked the maxima of the MO transitions. Using the same approach as in the previous sections, we have plotted the energy of the MO transitions against the thicknesses and deposition temperatures of the samples. This dependence is given in figure 5.16. Again, we can see that the energy of this transition rises with the deposition temperature - its value for the high-temperature samples is approximately 11% higher than that of the low-temperature samples.

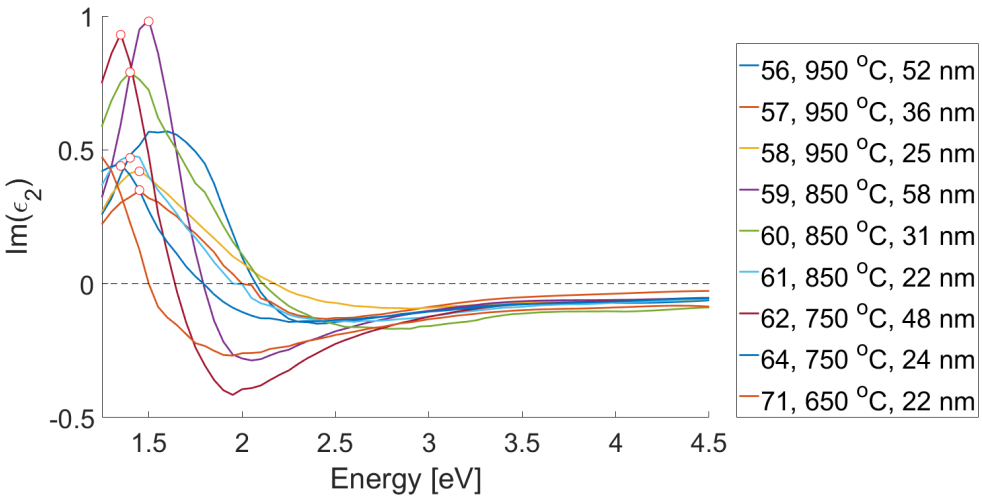

Figure 5.15: The spectral dependence of the imaginary part of ε_2 of the CFGG samples 56 through 71. The legend contains the number of the sample, its deposition temperature and thickness calculated from the optical response. The red circles represent the maximal values of the spectra.

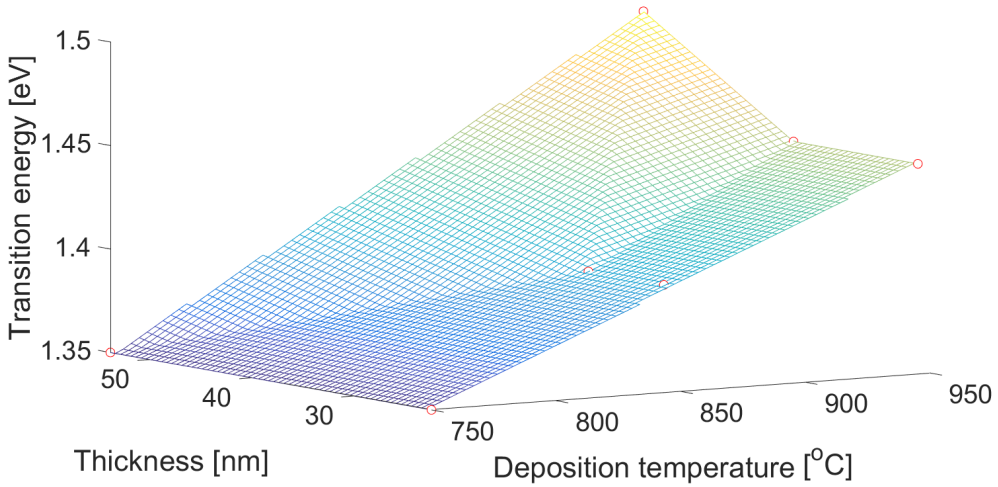

Figure 5.16: The energy of the peaks as a function of the deposition temperature and thickness of the CFGG samples. The red circles represent the width of the energy gap obtained from the analysis of the Im$\{\varepsilon_2\}$.

5.1.6 Magneto-optical magnetometry

Before we proceed to the explanation of the above-mentioned results based on ab-initio calculations, let us first present the results obtained via the Kerr magnetometer described in section 4.3.

The magnetometry of CFGG samples was measured in a polar geometry. The hysteresis loops are therefore considered for out-of-plane magnetization. An in-plane magnetization setup has been built as well and is currently being tuned for better precision. Following this work, in-plane magnetization curves will be measured on CFGG as well.

In figure 5.17 we show the Kerr hysteresis loops measured for CFGG samples. These loops were measured with the same electromagnet as we have used for the MO spectroscopy measurements. The magnet produces magnetic fields up to approximately 1.2 T. As we can see from figure 5.17, the samples did not achieve the full magnetic saturation in this field.

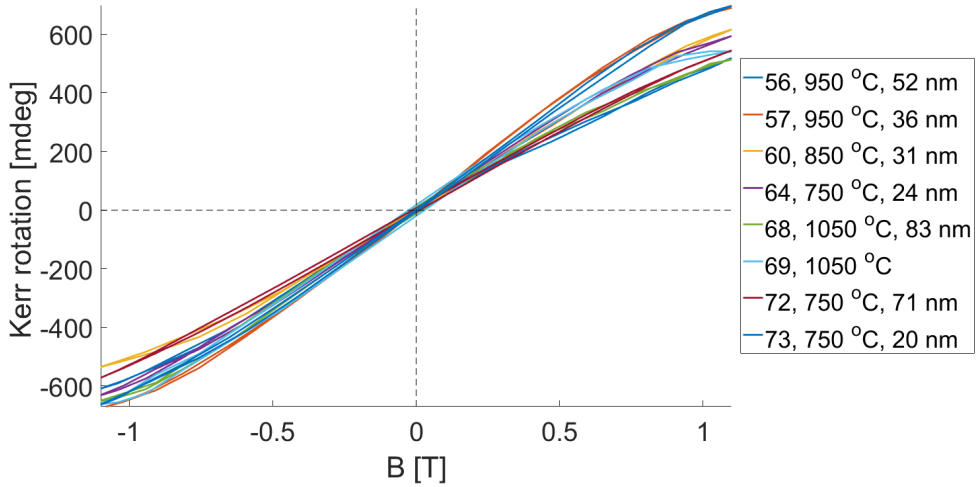

Figure 5.17: The Kerr loops of the CFGG compounds. The legend contains the number of the sample, its deposition temperature and thickness calculated from the optical response.

Vilanova et. al. has found in [41] that the saturation magnetization is unaffected by the change in deposition parameters for CFGG samples deposited at the temperature range from 450 ^{o}C to 750 ^{o}C. Although we have not reached saturation for our set of samples, we can see from the results presented in figure 5.17 that there is no apparent dependence either.

5.1.7 Ab initio calculations

To confirm the data interpretation provided above, a series of ab initio calculations was performed by Dr. Kudrnovsky at the Czech Academy of Sciences. The calculations were made in order to find the DOS of CFGG with various structural disorder.

In figure 5.18 the DOS for a perfectly ordered $L2_1$ CFGG can be found[2]. Using

[2]Calculated via generalized gradient approximations.

this result we can now interpret the results of the spectroscopic ellipsometry more thoroughly.

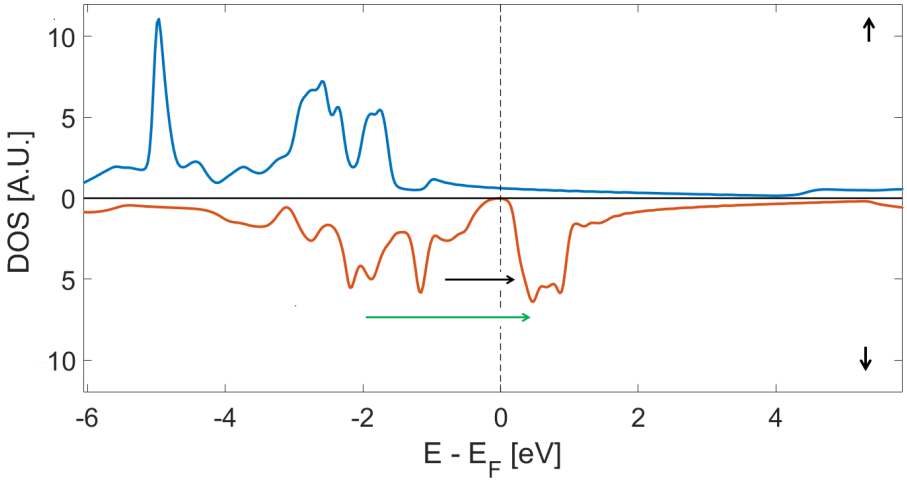

Figure 5.18: Spin-resolved density of states for a perfectly $L2_1$-ordered CFGG Heusler compound (exchange potential described by the generalized gradient approximation). Denoted by the blue line is the majority-spin DOS and by the red line the minority-spin DOS. The full line represents the zero line, while the dashed line the position of the Fermi energy. The black and green arrows denote the electron transitions visible in the spectra of diagonal permittivity.

As we can see from figure 5.18, there are two main transitions possible in the minority spin channel (denoted by black and green arrows). The lower energy transition (black arrow) corresponds to the lower-energy Lorentzian peak studied in section 5.1.4.

In the majority spin channel we can see the absence of the gap around the Fermi energy. Obviously, the spin-up electrons behave as conduction electrons at this part of the energy spectrum, hence contributing in a Drude-like behavior to the optical response of the material. This explains the rise of the permittivity shown in figure 5.7.

The densities of states for a perfectly B2-disordered and a perfectly DO_3-disordered have been calculated as well. In figure 5.19 we can see that the B2 structure preserves the minority-spin band gap, while DO_3 disorder completely suppresses it.

Finally, the magnetic moment of $L2_1$, B2 and DO_3 has been calculated and is listed in table 5.2.

Structure	m [μ_B per f.u.]
$L2_1$	5.507
B2	5.498
DO_3	5.536

Table 5.2: The calculated magnetic moment m for various types of disorder in CFGG.

We can see, that the DO_3 has been predicted to induce the highest moment of all the phases present in the sample set. The B2-type disorder seems to lower

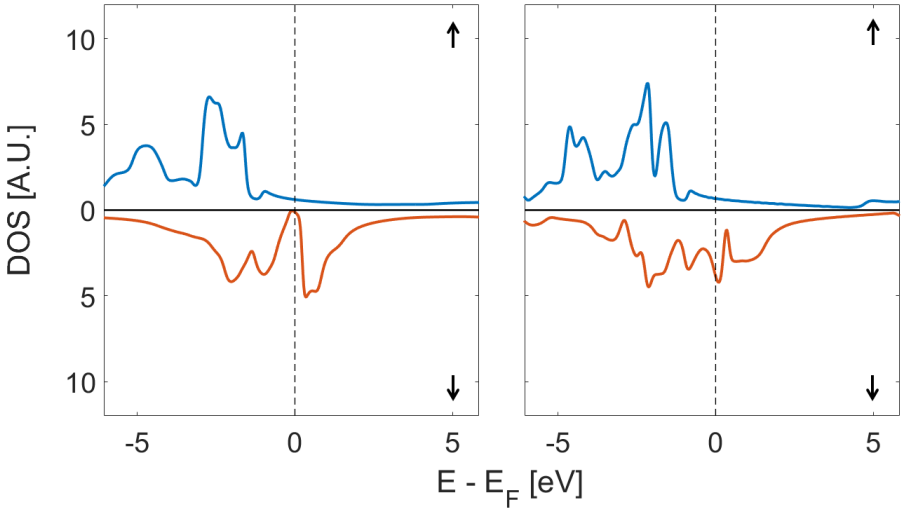

Figure 5.19: Spin-resolved density of states for a perfectly B2-disordered (left) and a perfectly DO_3-disordered (right) CFGG Heusler compound (GGA model). Denoted by the blue line is the majority-spin DOS and by the red line the minority-spin DOS. The full line represents the zero line, while the dashed line the position of the Fermi energy.

the magnetic moment of the compound, as well as $L2_1$. These results will become substantially important in the next section.

5.1.8 Summary of results

Let us now summarize and interpret the results obtained by all of the above-mentioned methods. The XRD results revealed that for thin CFGG samples deposited between 650 and 950 ^{o}C, the amount of the B2 phase lowers with the increasing deposition temperature. As the B2-disorder lowers, the amount of $L2_1$ and DO_3 phases rises. The XRD cannot, however distinguish between $L2_1$ and DO_3.

The spectroscopic ellipsometry has shown that one of the electron transitions shifts to higher energies as the deposition temperature rises. This can be explained with the help of the calculated DOS for B2 and $L2_1$ phases (see figure 5.20). As we can see, a transition from a completely B2-disordered compound to an $L2_1$-ordered one would widen the energy gap (denoted in the figure by black arrows).

According to the results of spectroscopic ellipsometry, the gap widens for samples deposited at higher temperatures. This is in accordance with the XRD results that show a decrease in the B2 phase present in the samples. This would also indicate that the amount of the $L2_1$ phase is actually increasing, rather than the DO_3 phase - a high amount of DO_3 would suppress the band gap.

From the ab initio calculations it follows that the magnetic moment of $L2_1$, B2 and DO_3 is approximately equal. Although, as shown by Kerr magnetometry, we have not achieved full saturation for the samples, it is reasonable to say that the magnetization of all of the phases will be the same. Despite this, the maximum Kerr rotation measured for each sample gradually lowers with the deposition

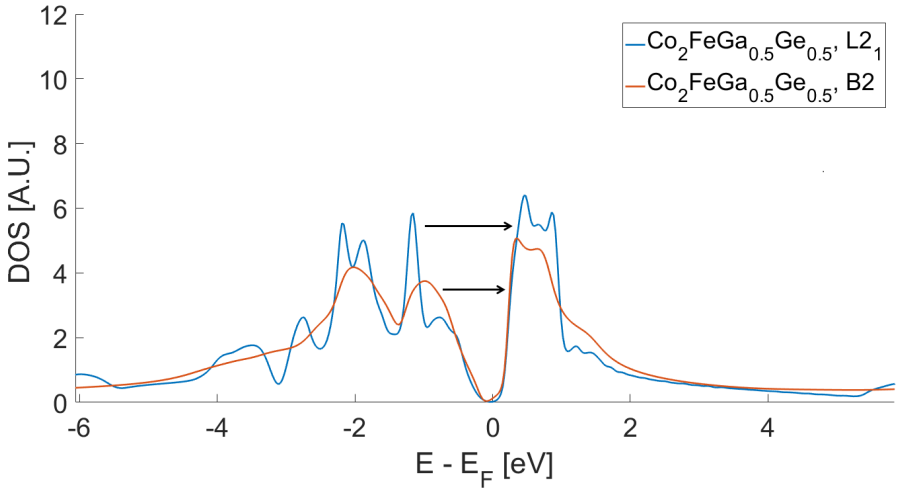

Figure 5.20: Comparison of the calculated minority-spin DOS for B2 and $L2_1$ phases of CFGG. Denoted by the blue line is the minority-spin DOS for a perfectly $L2_1$-ordered sample, while the red line represents the minority-spin DOS of a perfectly B2-disordered one. The black arrows denote the transition visible in the spectra of diagonal permittivity in the form of a Lorentzian peak.

temperature and sample thickness. This lowering may therefore be connected only to the changes in the linear MO tensor caused by the changes of the band structure of the samples. These changes are clearly visible in figure 5.16 were we see the widening of the MO gap with rising deposition temperature.

5.2 Fe_2MnGa

5.2.1 Sample description

Bulk samples of Fe-Mn-Ga (FMG) compounds were prepared by arc-melting in an Ar atmosphere using a Bühler MAM-1 furnace at the Institute of Physics, Czech Academy of Science (Dr. O. Heczko). The samples were annealed at 1000 ^{o}C in order to achieve good homogenization and subsequently at 800 ^{o}C to obtain $L2_1$ ordering.

Prior to the measurements, the samples were mechanically and electrolytically polished. The electrolytic polishing was performed using a 20% solution of nitric acid and methanol. This led to minimal roughness of the samples, which is required for optical and MO measurements.

In order to examine the influence of substituting Fe for the original nickel at the X-position, FMG samples with various Fe composition have been prepared. Hence, a unique sample set was made with the content of Fe varying between 1.46 and 1.95. Table 5.3 contains the exact stoichiometry of the FMG samples.

To compare the results obtained for FMG to the magnetic shape memory compound, Ni-Mn-Ga (NMG), a bulk sample of NMG has been produced by the group of Dr. Heczko as well. This reference sample was a perfectly stoichiometric Ni_2MnGa compound in an austenite phase. The sample has been annealed to achieve $L2_1$ ordering.

Number	Fe	Mn	Ga
2	1.87	0.97	1.17
4	1.95	0.97	1.08
6	1.46	0.94	1.60

Table 5.3: The stoichiometry of the FMG samples.

5.2.2 Spectroscopic ellipsometry

The varying content of Fe is expected to change the electron structure of the studied samples enormously. In order to investigate these changes and their dependence on the content of Fe in these compounds, we have performed a series of ellipsometric measurements. As it has been demonstrated in the previous section, these measurements and their evaluation can be used to probe the band structure of the material. For details concerning this experimental technique (well as the equipment used), see section 4.1.

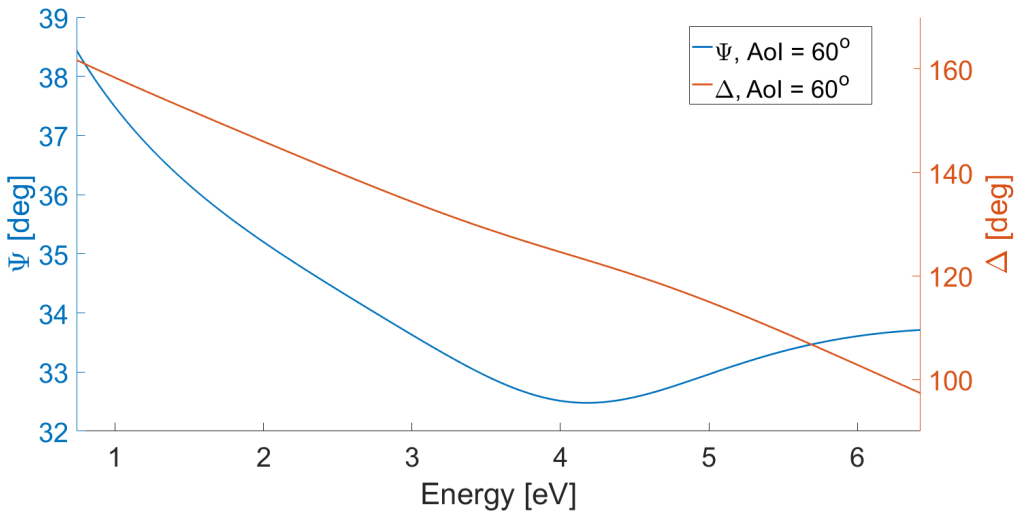

Figure 5.21: An example of the Ψ and Δ spectrum of a Fe-Mn-Ga compound. These are the results for sample 2, $Fe_{1.87}MnGa_{1.17}$, at an angle of incidence of 60^o.

Before each measurement, the samples had been cleaned using UV spectroscopy grade high-purity ethanol. Parameters Ψ and Δ have been measured in the reflective mode and the angles of incidence were 55^o, 60^o and 65^o. The spectral range of the incident light was between 0.8 to 6.5 eV. An example of the Ψ and Δ spectra is shown in figure 5.21 for sample 2.

The samples were modeled as a bulk FMG compound with a layer of Mn_2O_3 on top. The top layer has been added in order to account for the oxidation of the samples. The real and imaginary parts of the diagonal permittivity were calculated from the measured spectra of Ψ and Δ with the help of the Lorentz and Drude models.

In figures 5.22 and 5.23 we present the spectral dependence of the real and imaginary part of permittivity for each sample.

As we can see, the optical response of FMG rises in the NIR part of the spectrum in a Drude-like manner and gradually lowers towards higher energies. In

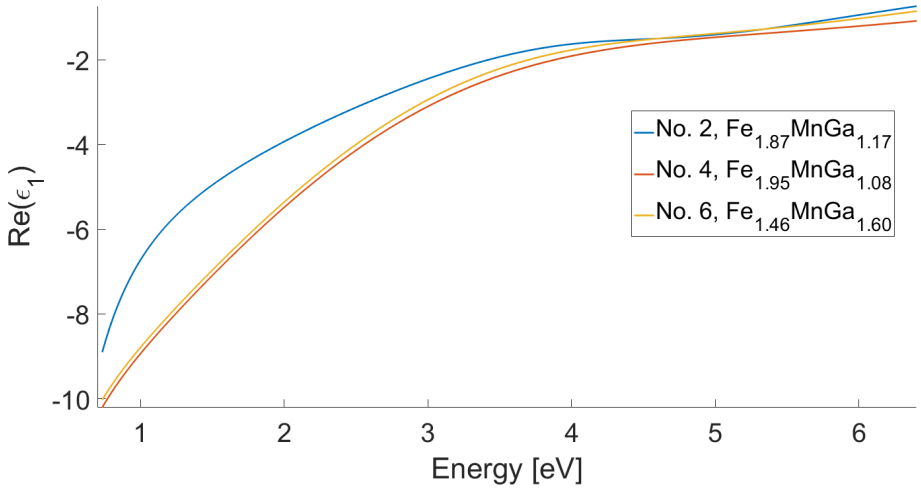

Figure 5.22: The spectral dependence of the real part of permittivity of FMG.

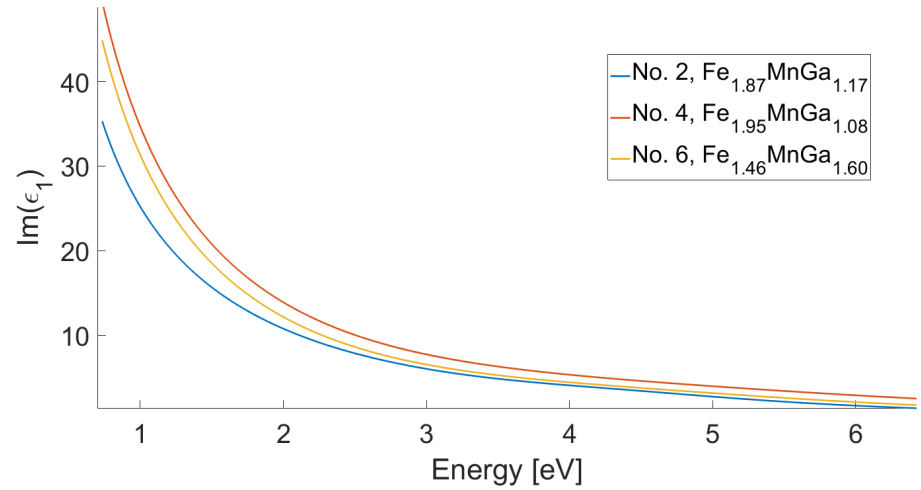

Figure 5.23: The spectral dependence of the imaginary part of permittivity of FMG.

the UV region it becomes almost negligible. There is also a Lorentzian transition at 4.5 eV. This peak is not clearly visible due to its wide bandwidth and low amplitude.

The amplitude of ε_1 is the highest for the sample number 4, which contains the highest amount of Fe across all of the FMG samples. The amplitude of ε_1 lowers for number 6, which contains the lowest amount of Fe and the it becomes the lowest for the sample number 2.

The spectral dependence of permittivity is obviously driven by free electrons. The dominant part of the spectrum is the Drude term, which indicates that the electrons behave as free carriers. This result can be explained by the presence of Fe in the samples, which increases the concentration to the concentration of free electrons.

5.2.3 Magneto-optical spectroscopy

In order to investigate the magneto-optical properties of the FMG compounds with varying Fe content, we have conducted a series of MO spectroscopy measurements in polar configuration. As in the previous section, these measurements should provide useful information about the electronic transitions in the samples.

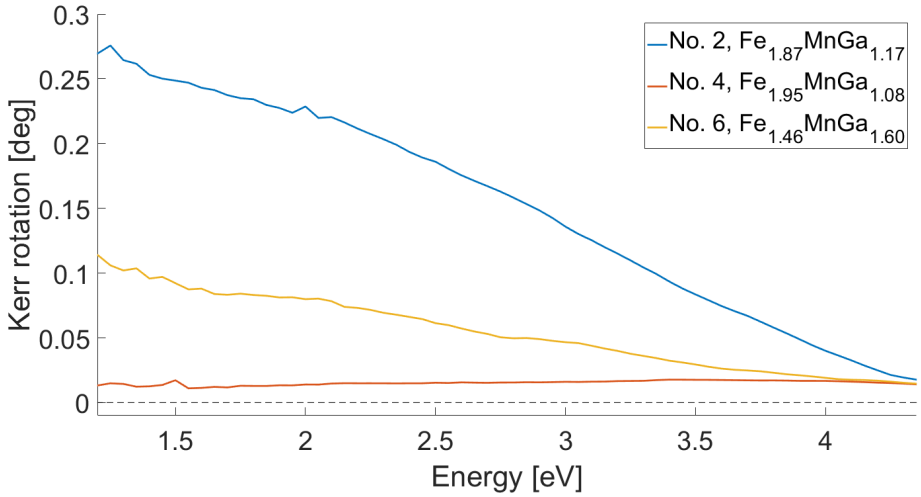

Figure 5.24: The spectral dependence of the the polar Kerr rotation of the FMG samples.

The investigated spectrum ranges from 1.5 to 4.5 eV. The samples were located in a magnetic field of approximately 1.14 T. In figures 5.24 and 5.25 we present polar Kerr rotation and Kerr ellipticity spectra. We see a similar behavior as in the ellipsometry case. The Kerr rotation rises in the NIR region a gradually lowers towards higher energies. The Kerr ellipticity, on the other hand, lowers in the NIR region and is the highest in the UV part of the spectrum. No spectral structures in the MO spectra can be seen.

For comparison, we present the Kerr rotation spectrum for the NMG sample (see figure 5.26). We can see multiple peaks at 1.5, 2.5 and 3.5 eV. The maximum response is up to 200 mdeg. The Kerr rotation changes the sign at approximately 2.8 eV.

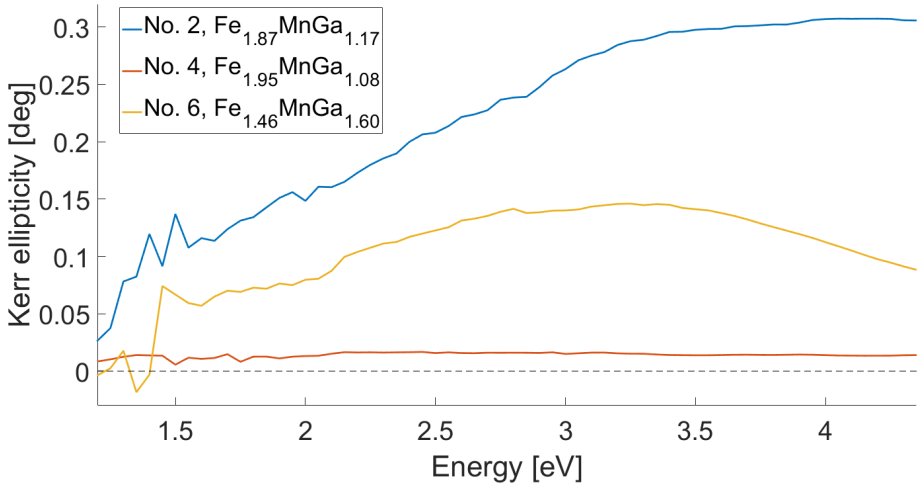

Figure 5.25: The spectral dependence of the the polar Kerr ellipticity of the FMG samples.

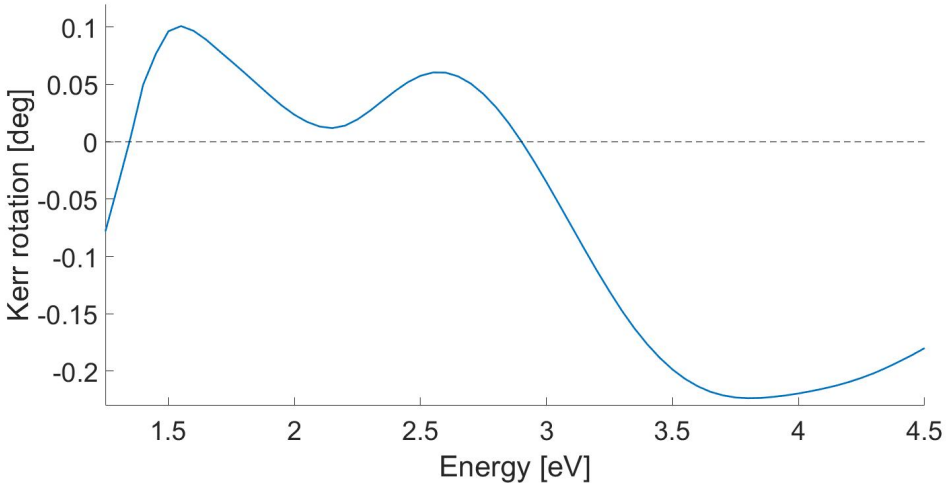

Figure 5.26: The spectral dependence of the the polar Kerr rotation for a stoichiometric NMG compound in an austenite phase.

The increase of Kerr rotation in the NIR region may be explained similarly to the interpretation of the ellipsometric data. The MO response may be entirely driven by the free electrons provided by the Fe atoms.

Unlike the NMG sample, the FMG does not exhibit any obvious spectroscopic features in the Kerr rotation spectra. Even the peak at 3.5 eV, that is typical for Heusler compounds with Mn as the Y element, is absent. It is possible that substituting Fe for Ni suppresses the Mn-driven electronic transitions entirely.

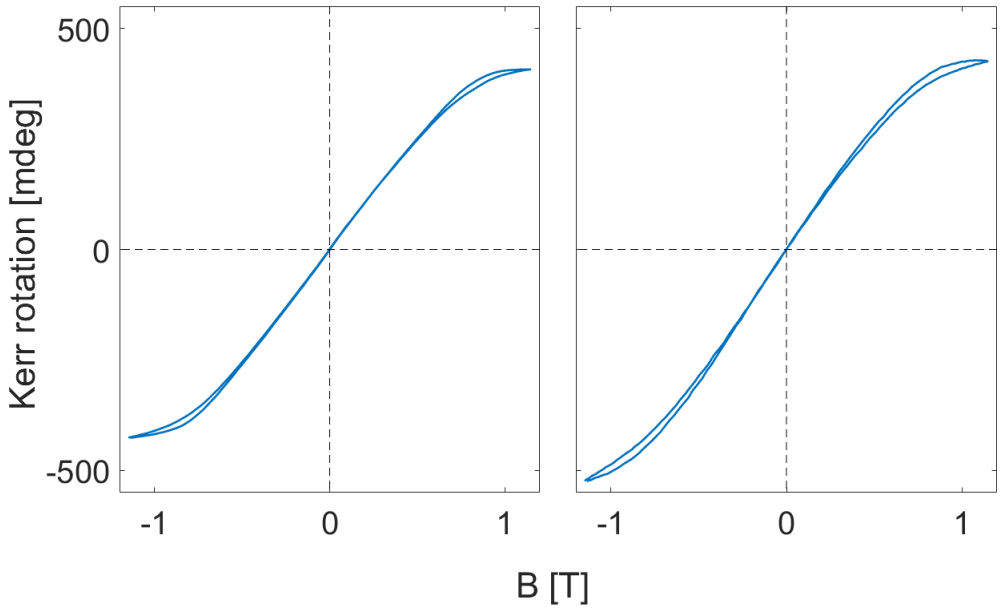

Figure 5.27: The Kerr loops measured for the Fe-Mn-Ga samples. Left: number 2 ($Fe_{1.87}MnGa_{1.17}$), right: number 6 ($Fe_{1.46}MnGa_{1.60}$).

5.2.4 Magneto-optical magnetometry

Using the method described in section 4.3, we have measured the Kerr hysteresis loops for samples 2 and 6. As it has been found in the previous section, sample 4 does not exhibit any MO response and therefore the Kerr loop could not be measured.

In figure 5.27 we present the polar Kerr loops measured for fields up to 1.2 T. Both samples are saturated at approximately 1.15 T. The coercive field is zero in both cases.

5.2.5 Summary of results

The MO properties of FMG differ noticeably from the original NMG Heusler compound. This is mostly due to the influence of Fe substitution of Ni on the electron structure. The presence of Fe in the compound causes higher concentration of free carriers. These carriers are responsible for the enhancement of both the optical and MO response in the NIR region, suggesting a full metallic behavior of the samples compared to half-metallic behavior of the NMG compound.

However, the amplitude of MOKE vanishes for higher energies and at 4.5 eV the Kerr rotation of FMG becomes almost negligible. In FMG there is no significant contribution of the Mn transitions to the MOKE spectra. The three MO peaks observed for NMG are absent in the FMG spectra, suggesting the suppression of the Mn involved transitions due to Fe substitution.

The sample with the highest content of Fe, $Fe_{1.95}MnGa_{1.08}$, has been found to posses no magnetic moment at all. Hence, its MO response is zero for all of the investigated spectral regions. For reasons given in section 3.2, this may suggest that this sample has antiferromagnetic ordering. It does, however posses the highest optical response in the NIR region.

The saturation magnetization is approximately equal for samples number 2 and 6, that is 1.15 T. Both samples exhibit ferromagnetic behavior with zero coercive field.

Conclusion

The aim of this thesis was to employ the optical and magneto-optical (MO) methods in the research of Heusler compounds. We have systematically studied the influence of the structural and composition changes of Heuslers on their electronic structure by the means of spectroscopic ellipsometry, MO spectroscopy and MO Kerr magnetometry. In addition to our experimental research, the ab initio calculations, as well as X-ray diffraction and atomic force microscopy measurements were included.

In the first part of the thesis, we have provided the theoretical background necessary for the successful experimental investigation of Heusler compounds as well as a rigorous interpretation of the obtained results. This part includes basic optical and MO theoretical approaches, characterization of the studied compounds and the description of the experimental techniques we have used.

In the second part, we have presented the results of our research. Two particular compounds have been studied - $CoFeGa_{0.5}Ge_{0.5}$ (CFGG) and Fe_2MnGa (FMG). In the case of the first compound, we have studied the manifestation of structural disorder in both optical and MO properties of the material. As for the second compound, we have investigated the effect of composition variation on its physical properties.

According to the results of atomic force microscopy, CFGG crystallizes in a column-like structure when the deposition temperature rises above 650 ^oC. The XRD measurements revealed the decline of the amount of the B2 disorder in the samples deposited above this temperature. The combined results of spectroscopic ellipsometry and MO spectroscopy show that this decline manifests itself through the shift of one of the peaks towards higher energies. Ab initio calculations have confirmed that this is indeed caused by the lower amount of B2 disorder in the material, as this leads to changes in the minority-spin gap. The ab initio analysis has further shown that the DO_3 disorder completely suppresses this gap. Since this has not been observed in the ellipsometric and MO spectra, we conclude that this type of disorder is not present in a significant amount. In summary, the CFGG samples deposited at higher temperatures contain a higher amount of the $L2_1$ ordering, which grown at the expense of the B2 phase. This change in structural order is detectable by both optical and MO methods. In addition, the out-of-plane hysteresis loops were measured and do not show any significant differences between the samples. Using the Kerr magnetometry, we have found that the saturation magnetization of all samples is above 1.2 T.

All FMG samples exhibited a large optical and MO response in the near infrared region. In this region, the amplitude of the diagonal permittivity rises in a Drude-like manner. This is probably caused by the free electrons introduced by the Fe atoms. The values of Kerr rotation rise for most samples as well, with the exception of the sample containing the highest amount of Fe. This composition has been found to completely suppress the magnetization of the material and produce no MOKE at all. Comparing our results with the ones obtained for a similar compound, Ni_2MnGa (NMG), we have found that the presence of Fe suppresses the transitions visible in the NMG spectra. The saturation magnetization for the remaining samples is approximately 1.15 T.

Bibliography

[1] Tanja Graf, Claudia Felser, Stuart S.P. Parkin, *Simple rules for the understanding of Heusler compounds*, Progress in Solid State Chemistry 39 (2011) 1-50.

[2] I. Aaltio, A. Sozinov *Giant Magnetorestrictive Materials*, Elsevier, 1st edition, 2016.

[3] Lukas Wollmann, Ajaya K. Nayak, Stuart S. P. Parkin and Claudia Felser, *Heusler 4.0: Tunable Materials*, arXiv:1612.05947, 1. 2. 2017.

[4] M. Jourdan, J. Minár, J. Braun, A. Kronenberg, S. Chadov, B. Balke, A. Gloskovskii, M. Kolbe, H.J. Elmers, G. Schönhense, H. Ebert, C. Felser and M. Kläui *Direct observation of half-metallicity in the Heusler compound* Co_2MnSi, arXiv:1612.05947, 1. 2. 2017.

[5] Roald K. Wangsness, *Electromagnetic Fields*, John Willey, New York 2nd edition, 1994.

[6] Jozef Kvasnica, *Teorie elektromagnetického pole*, Academia, Prague, 1st edition, 1985.

[7] Eugene Hecht, *Optics*, Addison Wesley, 4th edition, 2002.

[8] Max Born, Eugene Hecht, *Principles of optics*, Cambridge University Press, 7th edition, 1999.

[9] Justin Peatross, Michael Ware, *Physics of light and optics*, Brigham Young University, 2015 edition, 2015.

[10] Harland G. Tompkins, *Ellipsometry and polarized light*, Dover Publications, 1993.

[11] R. M. A. Azzam, N. M. Bashara, *Ellipsometry and polarized light*, North-Holland Publishing Company, 1st edition, 1977.

[12] Stefan Visnovsky, *Optics in Magnetic Multilayers and Nanostructures*, CRC Press, 1st edition 2006.

[13] Josef Kvasnica, *Matematický aparát fyziky*, Academia, 2nd edition, 1997.

[14] Miroslav Nyvlt, *Optical interactions in ultrathin magnetic film structures*, Doctoral thesis, Charles University Prague, 1996.

[15] Petr Malý, *Optika*, Karolinum, 2nd edition, 2013.

[16] Charles Kittel, *Introduction to solid state physics*, Academia, 1st edition, 1985.

[17] Alexandr S. Davydov, *Kvantová mechanika*, Nauka, 2nd edition, 1973.

[18] Jiří Formánek, *Úvod do kvantové teorie*, Academia, 1st edition, 1983.

[19] John J. Quinn, Kyung-Soo Yi, *Solid state physics - principles and modern applications*, Springer, 1st edition, 2009.

[20] Helmar Frank, *Fyzika a technika polovodičů*, SNTL, 1st edition, 1990.

[21] Peter Y. Yu, Manuel Cardona, *Fundamentals of semiconductors*, Springer, 3rd edition, 2005.

[22] Benjamin Balke, Sabine Wurmehl, Gerhard H Fecher, Claudia Felser and Jürgen Kübler, *Rational design of new materials for spintronics: Co_2FeZ (Z = Al, Ga, Si, Ge)*, Sci. Technol. Adv. Mater. 9 (2008) 014102

[23] Otto Litzman, Milan Sekanina, *Užití grup ve fyzice*, Academia, 1st edition, 1982.

[24] Jaroslav Hamrle, *Magneto-optical determination of in-depth magnetization profile in magnetic multilayers*, Doctoral thesis, Charles University Prague, 2003

[25] J Hamrle, S Blomeier, O Gaier, B Hillebrands, H Schneider, G Jakob, K Postava and C Felser, *Huge quadratic magneto-optical Kerr effect and magnetization reversal in the Co_2FeSi Heusler compound*, J. Phys. D: Appl. Phys. 40 (2007) 1563–1569.

[26] K. Postava, H. Jaffres, A. Schuhl, F. Nguyen Van Dau, M. Goiran, A.R. Fert, *Linear and quadratic magneto-optical measurements of the spin reorientation in epitaxial Fe films on MgO*, Journal of Magnetism and Magnetic Materials 172 (1997) 199-208.

[27] Š. Višňovský, *Magneto-optical permittivity tensor in crystals*, Czech. J. Phys. B 36 (1986).

[28] Claudia Felser, Atsufumi Hirohata, *Heusler Alloys*, Springer, 1st edition, 2016.

[29] Lukáš Beran, *Studium fyzikálních vlastností Heuslerových slitin*, Diploma thesis, Charles University Prague, 2015

[30] K. H. J. Buschow, P. G. van Engen and R. Jongebreur, Journal of Magnetism, *Magnetic and magneto-optical properties of Heusler alloys based on aluminium and gallium* , Magnetic Materials 38 (1983).

[31] R. A. de Groot, F. M. Mueller, P. G. van Engen, and K. H. J. Buschow, *New Class of Materials: Half-Metallic Ferromagnets*, Phys. Rev. Lett. 50, 2024 (1983).

[32] M. I. Katsnelson, V. Yu. Irkhin, L. Chioncel, A. I. Lichtenstein, and R. A. de Groot, *Half-metallic ferromagnets: From band structure to many-body effects*, Rev. Mod. Phys. 80, 315 (2008).

[33] Iosif Galanakis, *Slater-Pauling behavior in half-metallic magnets*, Journal of Surfaces and Interfaces of Materials, Volume 2, Number 1, 2014, pp. 74-78(5).

[34] Sabine Wurmehl, Gerhard H. Fecher, Hem Chandra Kandpal, Vadim Ksenofontov, Claudia Felser, Hong Ji Lin, *Investigation of Co_2FeSi: The Heusler compound with highest Curie temperature and magnetic moment*, Appl. Phys. Lett. 88, 032503 (2006).

[35] J. Kübler, G. H. Fecher, C. Felser, *Understanding the trend in the Curie temperatures of Co_2-based Heusler compounds: Ab initio calculations*, Physical Review B 2, 76 024414.

[36] Bradley A.J., Rogers J.W., *The Crystal Structure of the Heusler Alloys*, Proc. Roy. Soc. A144 (852): 340–359 (1934).

[37] Hem Chandra Kandpal, Claudia Felser and Ram Seshadri, *Covalent bonding and the nature of band gaps in some half-Heusler compounds*, J. Phys. D: Appl. Phys. 39 (2006) 776–785.

[38] Marc de Graef, Michael E. McHenry, Atsufumi Hirohata *Heusler Alloys*, Cambridge University Press, 2nd edition, 2007.

[39] Claudia Felser, Lukas Wollmann, Stanislav Chadov, Gerhard H. Fecher and Stuart S. P. Parkin, *Basics and prospective of magnetic Heusler compounds*, APL Materials 3, 041518 (2015).

[40] Aroyo, et. al., Zeitschrift fuer Kristallographie (2006), 221, 1, 15-27.

[41] E. Vilanova Vidal, H. Schneider and G. Jakob, *Influence of disorder on anomalous Hall effect for Heusler compounds*, Physical review. B, Condensed matter 83(17) (2011).

[42] H. S. Goripati, T. Furubayashi, Y. K. Takahashi and K. Hono, *Current-perpendicular-to-plane giant magnetoresistance using $Co2Fe(Ga_{1-x}Ge_x)$ Heusler alloy*, Journal of Applied Physics 113, 043901 (2013).

[43] J.C. Slonczewski, *Current-driven excitation of magnetic multilayers*, Journal of Magnetism and Magnetic Materials 159 (1996) 1-7.

[44] S. Li, Y. K. Takahashi, Y. Sakuraba, N. Tsuji and H. Tajiri, *Large enhancement of bulk spin polarization by suppressing Co_{Mn} anti-sites in $Co_2Mn(Ge_{0.75}Ga_{0.25})$ Heusler alloy thin film*, Appl. Phys. Lett. 108, 122404 (2016).

[45] Björn Hülsen, Matthias Scheffler and Peter Kratzer, *Thermodynamics of the Heusler alloy Co-Mn-Si: A combined density functional theory and cluster expansion study*, Phys. Rev. B 79 094407 2009.

[46] Yoshio Miura, Kazutaka Nagao and Masafumi Shirai, *Atomic disorder effects on half-metallicity of the full-Heusler alloys $Co_2Cr_{1-x}Fe_x)Al$: A first-principles study*, Phys. Rev. B 69 (2004), 144413.

[47] M. Aftab, G. Hassnain Jaffari, S. K. Hasanain and S. Ismat Shah, *Structural and magnetic properties of quaternary $Co_2Mn_{1-x}Cr_xSi$ Heusler alloy thin films*, Journal of Applied Physics 110, 053903 (2011).

[48] *https://chem.libretexts.org/Core/Physical_and_Theoretical_Chemistry/Spectroscopy/X-ray_Spectroscopy/EXAFS%3A_Theory*, 6.4. 2017

[49] J. M. Coey *Magnetism and Magnetic Materials*, Cambridge University Press, 4th edition, 2010.

[50] Farshad Nejadsattari, Zbigniew M. Stadnik, Janusz Przewoźnik, Kurt H. J. Buschow, *Mössbauer spectroscopy, magnetic and ab initio study of the Heusler compound Fe_2NiGa*, Physica B477 (2015), 113–122.

[51] S. Li, Y. K. Takahashi, T. Furubayashi and K. Hono, *Enhancement of giant magnetoresistance by $L2_1$ ordering in $Co_2Fe(Ge_0.5Ga_0.5)$ Heusler alloy current-perpendicular-to-plane pseudo spin valves*, Appl. Phys. Lett. 103, 042405 (2013).

[52] J. W. Jung, Y. Sakuraba, T. T. Sasaki, Y. Miura and K. Hono, *Enhancement of magnetoresistance by inserting thin NiAl layers at the interfaces in $Co_2FeGa_{0.5}Ge_{0.5}/Ag/Co_2FeGa_{0.5}Ge_{0.5}$ current-perpendicular-to-plane pseudo spin valves*, Appl. Phys. Lett. 108, 102408 (2016).

[53] Ikhtiar, S. Kasai, , Y. K. Takahashi, T. Furubayashi, S. Mitani and K. Hono, *Temperature dependence of magneto-transport properties in $Co_2Fe(Ga_{0.5}Ge_{0.5})/Cu$ lateral spin valves*, Appl. Phys. Lett. 108, 062401 (2016).

[54] S. Bosu, H. Sepehri-Amin, Y. Sakuraba, M. Hayashi, C. Abert, *Reduction of critical current density for out-of-plane mode oscillation in a mag-flip spin torque oscillator using highly spin-polarized $Co_2Fe(Ga_{0.5}Ge_{0.5})$ spin injection layer*, Appl. Phys. Lett. 108, 072403 (2016).

[55] Ye Du, T. Furubayashi, Y. K. Takahashi, Y. Sakuraba and K. Hono, *Polycrystalline CPP-GMR Pseudospin Valves Using 001 Textured $Co_2Fe(Ga_{0.5}Ge_{0.5})$ Layer Grown on a Conductive $(Mg_{0.5}Ti_{0.5})O$ Buffer Layer*, IEEE Transaction on Magnetics, vol. 51, no. 11, November 2015.

[56] I. Aaltioa, K.P. Mohanchandra, O. Heczko, M. Lahelin, Y. G, G.P. Carman, O. Söderberg, B. Löfgren, J. Seppälä, S. P. Hannula, *Temperature dependence of mechanical damping in Ni–Mn–Ga austenite and non-modulated martensite*, Scripta Materialia Volume 59, Issue 5, September 2008, Pages 550–553.

[57] T. Omori, K. Watanabe, R. Y. Umetsu, R. Kainuma and K. Ishida, *Martensitic transformation and magnetic field-induced strain in Fe–Mn–Ga shape memory alloy*, Appl. Phys. Lett. 95, 082508 (2009).

[58] Teuta Gasi, Ajaya K. Nayak, Michael Nicklas and Claudia Felser, *Structural and magnetic properties of the Heusler compound Fe_2MnGa*, Journal of Applied Physics 113, 17E301 (2013).

[59] W. Zhu, E. K. Liu, L. Feng, X. D. Tang, J. L. Chen, G. H. Wu, , H. Y. Liu, F. B. Meng and H. Z. Luo, *Magnetic-field-induced transformation in FeMnGa alloys*, Appl. Phys. Lett. 95, 222512 (2009).

[60] Y. V. Kudryavtsev, N. V. Uvarov, V. N. Iermolenko, J. Dubowik, J. Y. Rhee, Y. J. Yoo, Y. P. Lee, *Structural and Magnetic Properties, and Electronic Structures of Fe-Mn-Ga Alloys*, Journal of the Korean Physical Society, Vol. 62, No. 10, May 2013, pp. 1508-1513.

[61] X. D. Tang, W. H. Wang, W. Zhu, E. K. Liu, G. H. Wu, *Giant exchange bias based on magnetic transition in γ-Fe2MnGa melt-spun ribbons*, Appl. Phys. Lett. 97, 242513 (2010).

[62] A. Sozinov, N. Lanska, A. Soroka and W. Zou, *12% magnetic field-induced strain in Ni-Mn-Ga-based non-modulated martensite*, Appl. Phys. Lett. 102, 021902 (2013).

[63] Ladislav Straka, *Magnetic and magneto-mechanical properties of Ni-Mn-Ga magnetic shape memory alloys*, Doctoral thesis, Helsinki University of Technology, Helsinki, 1996.

[64] Enrique Vilanova Vidal, *Influence of defects and disorder on anomalous Hall effect and spin Seebeck effect on permalloy and Heusler compounds*, Doctoral thesis, Johannes Gutenberg University in Mainz, Mainz, 2007.

List of Figures

List of Tables